***Snrpb*, the gene mutated in CCMS, is haploinsufficient and required in neural crest cells for proper splicing of developmentally important genes essential for craniofacial morphogenesis**

Sabrina Shameen Alam[1,2], Shruti Kumar[1,2], Marie-Claude Beauchamp [1], Eric Bareke [2], Alexia Boucher[1,3], Nadine Nzirorera[1,2], Reinnier Padilla[2], Si Jing Zhang[2], Jacek Majewski[2], Loydie A. Jerome-Majewska [1,2,3,4*]

[1] Research Institute of the McGill University Health Centre at Glen Site, Montreal, QC, H4A 3J1, Canada

[2] Department of Human Genetics, McGill University, Montreal, QC, H3A 0G1, Canada

[3] Department of Anatomy and Cell Biology, McGill University, Montreal, QC, H3A 2B2, Canada

[4]Department of Pediatrics, McGill University, Montreal, QC, H4A 3J1, Canada

*Correspondence: loydie.majewska@mcgill.ca

Summary:

Heterozygous mutations in *SNRPB*, an essential core component of the five small ribonucleoprotein particles of the spliceosome, are responsible for Cerebrocostomandibular Syndrome (CCMS). However, the underlying pathophysiology of CCMS remains a mystery. We generated mouse embryos with heterozygous deletion of *Snrpb* and showed that they arrest shortly after implantation. We also showed that heterozygous deletion of *Snrpb* in the developing brain and neural crest cells models many of the craniofacial malformations found in CCMS, and results in death shortly after birth. Abnormalities in these mutant embryos ranged from cleft palate to a complete absence of the ventral portion of the face and are due to apoptosis of the neural crest cells in the frontonasal prominence and pharyngeal arches. RNAseq analysis of mutant embryonic heads prior to morphological defects revealed increased exon-skipping and intron-retention in association with increased 5' splice strength. Mutant embryonic heads had increased exon-skipping in *Mdm2* and *Mdm4* negative regulators of the P53-pathway and a increased nuclear P53 and P53-target genes. However, removing one or both copies of *P53* in *Snrpb* heterozygous mutant neural crest cells did not rescue craniofacial development. We also found a small but significant increase in exon-skipping of several transcripts required for head and midface development, including *Smad2* and *Rere*. Furthermore, mutant embryos exhibited ectopic or missing expression

of *Fgf8* and *Shh*, which are required to coordinate face and brain development. Thus, we propose that mis-splicing of transcripts that regulate P53-activity and craniofacial-specific genes both contribute to craniofacial malformations.

Keywords: Cerebrocostomandibular syndrome (CCMS); *SNRPB*; splicing; spliceosomopathies, neural crest cells (NCCs); craniofacial

INTRODUCTION

95% of human pre-mRNAs are alternatively spliced to generate multiple mRNAs (Chen and Manley, 2009; Nilsen and Graveley, 2010) thus increasing the number and diversity of proteins expressed from the human genome. The major spliceosome or U2-dependent spliceosome catalyses 99% of RNA splicing reactions in human (Wickramasinghe *et al*., 2015), while the minor or U12-dependent spliceosome is responsible for splicing of approximately 700 minor introns in 666 genes (Olthof *et al.*, 2019). The major spliceosome is composed of U1, U2, U5, and U4/U6 small nuclear ribonucleoprotein proteins (snRNPs) named for their core associated small RNAs (snRNAs). *SNRPB* encodes SmB and SmB' which are core components of the spliceosome. SmB/B' help to form the heptameric ring on the U snRNAs of the five snRNPs of the major spliceosome. Several groups have reported heterozygous mutations inof *SNRPB* in patients with Cerebrocostomandibular Syndrome (CCMS, OMIM# 117650) (Lynch *et al.*, 2014, Barcot *et al.*, 2015, Tooley *et al.*, 2016). CCMS patients have rib gaps and narrow chests, and craniofacial defects such as malar hypoplasia and micrognathia, with variable expressivity (Beauchamp *et al.*, 2020) and incomplete penetrance.

In addition to the two coding transcripts, SmB and SmB', *SNRPB* also encodes for a third premature termination codon (PTC) containing transcript that is predicted to undergo non-sense mediated decay. Most mutations found in CCMS patients increase inclusion of the PTC containing alternative exon 2 leading to no change or reduced levels of the coding transcripts in patient's fibroblasts (Barcot *et al.*, 2015 and Lynch *et al.* 2014). However, though it is presumed that increased expression of the PTC-containing transcript leads to reduced levels of SmB/SmB' in all CCMS patients, reduced levels of SNRPB protein has not been reported in any CCMS patient

cells. We postulated that a mouse model carrying mutation in *Snrpb* can be used to understand the role of *Snrpb* during embryogenesis and shed insight into the pathophysiology of CCMS.

Towards this goal, we generated a conditional mutant mouse line with *loxP* sequences flanking the genomic region that encompasses exons 2 and 3 of *Snrpb*. Using β-actin-cre we showed that widespread heterozygous deletion (*Snrpb*$^{+/-}$) of these exons reduced levels of *Snrpb* and resulted in embryonic arrest by embryonic (E) 9.5. To investigate the role of *Snrpb* specifically during craniofacial development, we used *Wnt1-Cre2* to generate *Snrpb* heterozygosity in the developing brain and neural crest cells (*Snrpb*$^{ncc+/-}$). We showed that a subset of these embryos survived to birth and died shortly after. Most *Snrpb*$^{ncc+/-}$ mutant embryos die between E17.5 and birth, with brain and craniofacial defects of variable expressivity. RNAseq analysis of the E9.0 embryonic heads of *Snrpb*$^{ncc+/-}$ mutants before morphological defects were apparent, revealed a significant increase in differential splicing events (DSE), but few differentially expressed genes (DEGs). Pathway analysis indicated that these DEGs were associated with the spliceosome and the P53-pathway. However, although nuclear P53 and apoptosis were increased in *Snrpb*$^{ncc+/-}$ embryos, reducing levels of P53 genetically in the neural crest did not rescue craniofacial defects in these mutants. Intriguingly, a number of DSE were found in genes important for craniofacial development. Furthermore, the expression of *Shh* and *Fgf8* which forms the facial organizer was disrupted in the craniofacial region. Our findings support disrupted splicing as the major driver of abnormalities in *Snrpb* mutant embryos. We suggest that abnormal splicing of genes important for craniofacial development results in an additive effect that disrupts morphogenesis of the head and brain.

RESULTS

Mouse embryos with deletion of exons 2 and 3 of *Snrpb* (*Snrpb*$^{+/-}$) have reduced levels of *Snrpb* and die post-implantation

To test if reduced levels of *Snrpb* in mouse recapitulates abnormalities found in CCMS patients, we first generated a conditional mutant mouse line with *loxP* sequences in intron 1 and intron 3 of the gene. We then used β-actin-cre to delete the *loxP*-flanked region – exon 2, the PTC encoding alternative exon 2, and exon 3 of *Snrpb* (Figure 1A) – to produce *Snrpb* heterozygous mice (*Snrpb*$^{+/-}$). However, no *Snrpb*$^{+/-}$ mice were found at birth (P0) or at weaning, indicating that

these mutants died before birth (data not shown). To determine when *Snrpb*$^{+/-}$ embryos die, we dissected pregnant females from E6.5 – E10.5. We found that mutant *Snrpb*$^{+/-}$ embryos were undergoing resorption by E9.5 and were all dead by E10.5 (data not shown). We confirmed that *Cre*-mediated deletion of the *loxP*-flanked region generated a shorter *Snrpb* transcript of 527 bp (Figure 1B) and resulted in a statistically significant 70% reduction in levels of *Snrpb* in E8.5 *Snrpb*$^{+/-}$ embryos (p= 0.0052, T-Test) (Figure 1C). Thus, deletion of exons 2 – 3 of *Snrpb* leads to a significant reduction in *Snrpb* level in heterozygous mutant embryos. Our data indicate that the amount of functional protein expressed by a single wild-type allele of *Snrpb* was insufficient for embryonic growth and survival post-implantation.

Snrpb is required in the neural crest cells for craniofacial development and postnatal survival

We next used a *Wnt1-Cre2* transgene to delete *Snrpb* in the neural tube and neural crest cells (*Snrpb*$^{ncc+/-}$) to examine its role during craniofacial development. No *Snrpb*$^{ncc+/-}$ mutant pups were found at postnatal day (P)1 and P21 (p>.0001, chi-square). At P0, we recovered 5 heterozygous *Snrpb*$^{ncc+/-}$ pups from 6 litters (n=47). Most had no visible milk spots, indicating that they failed to feed (n=4/5). One *Snrpb*$^{ncc+/-}$ pup was normal, while the rest had microcephaly, abnormally shaped heads, short snouts, and small outer ears (n=4) (Figure 1D-F). To determine when *Snrpb* is first required in neural crest cells for craniofacial development we mated *Snrpb* conditional heterozygous and *Wnt1-cre2* heterozygous mice and collected and analyzed embryos from E9.0 and E17.5. At E9.0, *Snrpb*$^{ncc+/-}$ embryos with thirteen or less somites, were indistinguishable from control (*Snrpb*$^{+/+}$ or *Wnt*$^{tg/+}$) littermates (Figure S1A). Morphological abnormalities were first apparent in 45% of E9.5 *Snrpb* $^{ncc+/-}$ mutants (n=33), and this number increased to 75% by E10.5 (n=57). At these stages, abnormal *Snrpb*$^{ncc+/-}$ embryos exhibited hypoplasia of the midbrain and hindbrain. In the ventral region, mutant embryos showed hypoplasia to a complete absence of forebrain, frontonasal prominence, and pharyngeal arches (Figure S1 B-C).

At E11.5, abnormal *Snrpb*$^{ncc+/-}$ embryos (n= 12) could be sorted into three groups. We assigned the 16% of embryos, which were indistinguishable from wild type, to Group 1; the 12% of mutant with hypoplasia of the developing brain, face and head were assigned to group 2; and the remaining 66% were assigned to group 3. Abnormalities found in group 3 included hypoplasia of the midbrain, an abnormally enlarged forebrain, sub-epidermal swelling, an absence of the

frontonasal and the maxillary prominences, and a hypoplastic mandibular arch (Figure S1D). At E12.5 (n= 14), a fourth phenotypic group comprising 21% of *Snrpb*$^{ncc+/-}$ embryos was found. Embryos in this group showed a complete absence of the ventral portion of the head and face, edema in the head, and a hypoplastic mandibular arch (Figure S1E right panel). 29% of *Snrpb*$^{ncc+/-}$ embryos were morphologically normal (group 1), 21% and 29% of *Snrpb*$^{ncc+/-}$ embryos were classified as group 2 and group 3, respectively. Mutants in group 2, exhibited clefts in the frontonasal prominence and the mandible, while those in group 3, had hypoplasia of the midbrain, an abnormal forebrain, and cleft of the hypoplastic frontonasal and maxillary prominences (Figure S1E).

At E14.5, 29% of *Snrpb* embryos were dead (n=5/17). Morphologically normal *Snrpb*$^{ncc+/-}$ embryos comprised 8% of live mutant embryos (n=12). Mutant embryos in group 2 (n=3), had a hypoplastic pinna, a dome-shaped head, and nasal clefts; and those in group 3 (n=4), showed hypoplasia and cleft of the frontonasal, maxilla and mandibular regions, and sub-epidermal edema (Figure 1G, S1F). *Snrpb*$^{ncc+/-}$ embryos in group 4 (n=4) showed the most severe abnormalities (Figure 1G, S1F), with a complete absence of the ventral portion of the head and face. At E17.5 25% of *Snrpb*$^{ncc+/-}$ embryos were found dead (n=4/16), like what was observed at E14.5. However, amongst live mutants (n=12) we did not observe any phenotypically normal embryos. At this stage, half of the mutant embryos found were classified as group 2, (n=6) and the number of mutant embryos in groups 3 (n= 4) and 4 (2), were similar to what was found at E14.5 (Figure 1H, S1G). Thus, wild-type levels of *Snrpb* are critical in the neural crest cells from E9.5 onwards for normal development of the head and face. Furthermore, though *Snrpb*$^{ncc+/-}$ mutants can survive to birth, a substantial proportion of these mutants die between E14.5 and birth.

Snrpb is required in neural crest cells for proper differentiation of both mesoderm and neural crest cells-derived cartilage and bones

Skeletal preparations with Alcian blue to stain cartilage and alizarin red to stain bone were used to examine development of neural crest cell derivatives in the developing head and face at E14.5, E17.5, and P0. In *Snrpb*$^{ncc/+}$ E14.5 and E17.5 embryos belonging to groups 2 and 3, the mesoderm-derived parietal bone (n=8) and the intraparietal bone – which is derived from both mesoderm and neural crest cells – were hypoplastic (Figure 2A, S2A-B). Neural-crest derived bones such as the temporal and alisphenoid bones were missing, while the frontal and nasal bones

were hypoplastic (n= 5) (Figure 2B, S2). Mutant embryos in these two groups also showed clefts of the nasal and pre-maxillary cartilages and bones, the palate, as well as hypoplasia of Meckel's cartilage and its derivative, the mandible (Figure 2C, 2D and S2). The zygomatic arch also failed to form in group 3 mutants (Figure 2B). Those heterozygous mutants belonging to group 4 had hypoplasia of the basisphenoid bone and all neural crest cell-derived cartilage or bone elements normally found on the ventral surface of the head and face (Figure 2B and S2). The one P0 *Snrpb*$^{ncc+/-}$ pup belonging to group 1, was indistinguishable from controls. Group 2 P0 *Snrpb*$^{ncc+/-}$ pups exhibited a range of skull defects, including heterotopic ossification in the frontal suture (n=1), a hypoplastic and asymmetric basisphenoid, and reduced size of the squamous part of the temporal bone (n = 3) (Figure S3).

Though the lower jaws formed in E14.5 and E17.5 *Snrpb*$^{ncc+/-}$ mutants in groups 2 and 3, they were both asymmetrical and bilaterally smaller when compared to those of wild-type embryos (Figure 2D, T-test, $p<.0001$). The mandible was hypoplastic but connected at the distal end, and proximal structures such as the coronoid and the condylar processes failed to form (Figure 2C). Additional defects found in mutant embryos included partial ectopic cartilage in the proximal end of Meckel's cartilage, missing tympanic ring, hypoplasia or absence of the hyoid, and missing tracheal cartilages. In addition, ectopic cartilages, which could not be conclusively identified (n=4 of 7) (Figure 2E, S2C) were also found in the middle ear. Palatine defects including clefts in the premaxilla, missing palatine shelves, (Figure S3A) and a curved premaxilla were found in group 2 P0 *Snrpb*$^{ncc+/-}$ mutants (n=4). Meckel's cartilage and the lower jaw which forms around it were also asymmetric in these mutants. Specifically, the condyloid and the angular processes were shortened bilaterally (n=1), while the angular process was asymmetric in the other three mutants, with 1 showing a wider angular process (Figure S3B). We also saw middle ear defects such as absent, or abnormally shaped tympanic ring, and presence of ectopic ossification in all four mutants (Figure S3C).

Derivatives of cranial, cardiac, and trunk neural crest cells are abnormal in *Snrpb* mutants

In addition to cartilage and skeletal abnormalities, the dorsal root ganglia, and cranial nerve ganglion – which form from ectodermal placodes and neural crest cells – were also abnormal in *Snrpb*$^{ncc+/-}$ mutants. Neurofilament staining of *Snrpb*$^{ncc+/-}$ mutant embryos showed that the cranial ganglia were reduced in size, and all had abnormal neuronal projection into the pharyngeal arches

(n=2) (Figure 3A). The ophthalmic project of the trigeminal nerve (CN V) was reduced and did not extend over the lens, the maxillary projection appeared disorganized and missing, while the mandibular projection was reduced and appeared to have formed ventral to the first arch. In addition, an ectopic projection was found in CN V in mutants. Furthermore, the proximal portions of the geniculate (CN VII) and vestibulo-acoustic (CN VIII) ganglia were thicker than in control. Similarly, the glossopharyngeal nerve (CN IX) was abnormally thicker in the proximal region before the pharyngeal arch, had ectopic projection into pharyngeal arch 2, and reduced projection into pharyngeal arch 3. Finally, the proximal portion of the vagus nerve (CN X) was relatively normal but had an abnormal bundle at the distal end with reduced projections into the heart. Furthermore, the dorsal root ganglia which are derived from trunk neural crest cells were reduced in size and bifurcated at the proximal end (Figure 3B).

Micro CT scans of a morphologically normal (group 1) E17.5 *Snrpb*$^{ncc+/-}$ embryo revealed that the aorticopulmonary septum which is derived from cardiac neural crest cells failed to differentiate in E17.5 *Snrpb*$^{ncc+/-}$ embryos (Figure S4B-S4E). Furthermore, the thymus gland, a derivative of the third pharyngeal pouch, also failed to form in this mutant embryo (Figure S4F). Micro CT analysis also revealed additional internal defects. In an E14.5, *Snrpb*$^{ncc+/-}$ embryo from group 4, the nasal septum and nasopharyngeal cavity were not formed, however, the oropharynx, tongue and pituitary gland were present (Figure S4A). Finally, in E12.5, E14.5 and E17.5 mutant embryos, the cerebral cortex was abnormally thin, and the lateral ventricles were enlarged (Figure S4). Altogether, our morphological analysis indicates that *Snrpb* is required for the formation of structures that are derived from or induced by neural crests along the anterior-posterior axis. Our data also suggest that cardiac anomaly may be responsible for the death of morphologically normal *Snrpb*$^{ncc+/-}$ embryos, such as the one found at P0.

Neural crest cells require wild-type levels of *Snrpb* for their survival in the craniofacial region

To track *Snrpb*$^{ncc+/-}$ heterozygous neural crest cells and their derivatives, we introduced the ROSA lacZ (Soriano P, 1999) and ROSA mT/mG (Mazumdar *et al.*, 2007) reporters into our mutant line. At E9.5, wild-type and *Snrpb*$^{ncc+/-}$ embryos (morphologically normal and abnormal) showed a comparable number of X-Gal positive mutant cells in the head and pharyngeal arches (Figure S5A-C) with no statistically significant differences (n=3). However, at E10.5,

morphologically abnormal mutant embryos (n=4) showed a reduced proportion of X-Gal positive cells in the developing head region (Figure 3C-D), and this difference was statistically significant when compared to wild type (T-test, p=.003). To determine if reduced proliferation and/or increased apoptosis contribute to loss of X-Gal positive *Snrpb* heterozygous cells at E10.5, Phosphohistone H3 immunostaining and TUNEL assay, respectively, were performed. No significant changes in proliferation were found at E9.5 and E10.5 (Figure S5 J-K). However, a statistically significant increase in TUNEL positive cells was found in the developing head region of E9.5 *Snrpb*$^{ncc+/-}$ embryos (T-test, p=.029) when compared to controls (Figure 3E). Our data indicate that *Snrpb* heterozygous cells migrate into the developing head region and the pharyngeal arches. However, a subset of these cells undergoes apoptosis and are lost in mutant embryos by E10.5.

Mutations in *Snrpb* cause an overall increase in both skipped exon (SE) and intron retention (IR)

To identify the molecular events that precede cell death in *Snrpb*$^{ncc+/-}$ embryos, head of E9.0 embryos with 11-13 somite pairs were isolated and used for RNA sequencing analysis. Surprisingly, gene expression data did not reveal a major distinction between mutant and control embryos and the samples did not cluster by genotype. This was further corroborated by differential gene expression (DEG) analysis, which identified very few (76) DEGs: 50 upregulated and 26 downregulated in the mutant embryos. This low number of DEGs is consistent with the lack of a clear phenotypic distinction at this developmental stage. However, the DEGs which were identified could already be characterized into relevant molecular pathways, specifically belonging to the P53 signaling pathway and representing components of the spliceosome (Figure 4A).

In contrast to the low number of DEGs, a large number of transcripts were found to be abnormally spliced. We identified 722 significant (FDR = 0.1) differentially spliced events (DSE) between the *Snrpb*$^{ncc+/-}$ (Het) and wild-type (WT) samples. The most abundant of these DSE were skipped exons (SE) and retained introns (RI) (Figure 4B). While the high proportion of SE could be expected based on prior alternative splicing studies, it was notable that more than 30% of the total AS events detected were RI events. We observed a strong tendency towards increased exon skipping and intron inclusion in the mutant samples; there were more SE (273 in Het versus 83 in WT) and RI (191 in Het versus 21 in WT) (Figure 4B). Consistent with the absence of significant

gene expression changes, DSEs in *Snrpb*$^{ncc+/-}$ embryos did not lead to significant changes in inclusion of PTC containing exons or introns (Figure S6 A-D). However, SEs were more likely to be alternative exons (non-constitutive) in heterozygous (p=0.0034) versus wild type (Figure 4C-D), and expression of transcripts with splicing of constitutive exons was significantly reduced in mutants (p=0.0035) when compared to wild type (Figure 4E-F). Those global trends in splicing are consistent with those previously found in cell culture, suggesting that SNRPB deficiency results in increased skipping of alternatively spliced exons resulting from reduced recognition of splicing signals (Correa *et al.*, 2016).

Increased skipped exon (SE) and intron retention (IR) in *Snrpb* mutants are not linked to identifiable sequence features

We next investigated whether the aberrant splicing events in the mutant embryos could in fact be characterized by specific sequence features. We compared alternative events preferentially found in the mutants to two control groups: 1) events preferentially found in the wild-type embryos, and 2) a set of 1000 randomly chosen alternative events. Specifically, we aimed to test whether aberrant events in the mutants were associated with weaker splice signals. While there was a very slight trend towards weaker splice site scores (MaxEntScan, Yeo *et al.*, 2004) of RI in mutant embryos as compared to the controls, the differences were small and not statistically significant (Figure S6E-F). In contrast 5' SS strength was significantly higher in *Snrpb*$^{ncc+/-}$ heterozygous embryos when compared to controls (Figure 4G), while the 3' SS was comparable between mutants and controls (Figure 4H). We also analyzed the strength and position of predicted branch point (BP) signals (LaBranchoR, Paggi and Bejerano, 2018), but again we did not find notable differences (Figure S6K-N), with the exception of a slight preference for a more distal branch point location of mutant-specific SE events (27 bp in mutant versus 25 bp in the random set, p= 0.026). We also looked at general base composition in SE and RIs and no statistically significant difference was observed (Figure S6O-R), though the GC content in retained introns was slightly increased (Figure S6S-T). We also found no statistical differences in the length of SEs and RIs, although RIs were generally shorter in mutants when compared to wildtype (data not shown). Finally, we scanned for the frequency of RNA-binding protein motifs around the mutant specific events (rMAPS2, Jae Y Hwang *et al.* 2020), but did not identify significant enrichment of recognition signals of known splicing factors.

Overall, we did not find a compelling indication that the splicing aberrations present in mutants are linked to identifiable sequence features. The slight preference for stronger 5' SS, branch point site location (BPS) and intronic nucleotide composition are notable but will need further scrutiny using more sensitive experimental designs. However, pathway analysis indicated that DSEs genes were significantly associated with mRNA processing (Figure 4K). Thus, the relatively large number of splicing aberrations, as compared to differentially expressed genes, detected at this developmental stage supports the hypothesis that these general splicing defects precede aberrations in gene expression and initiate the molecular cascade that leads to phenotypic changes.

Increased skipping of *Mdm2* exon 3 and *Mdm4* exon 7, key regulators of P53, are associated with increase nuclear P53 in heads of *Snrpb*$^{ncc+/-}$ embryos

We next investigated the key splicing changes that could explain craniofacial malformations in *Snrpb*$^{ncc+/-}$ embryos. We found increased skipping of exon 3 of *Mdm2* and exon 7 of *Mdm4,* regulators of the P53 pathway in our RNA-Seq analysis and confirmed these increases by RT-PCR (Figure 5A-B). Increased skipping of these exons was previously reported in cultured *Snrpb* knockdown cells and shown to increase levels of nuclear P53 in mouse embryos with mutations in *Eftud2* a core component of the spliceosome (Beauchamp *et al.,* 2021, Alstyne *et al.,* 2018, Correa *et al.,* 2016). Immunohistochemistry with an antibody to P53 revealed a significant enrichment of nuclear P53 in E9.5 mutant heads (Figure S7A-B). Furthermore, levels the P53-regulated genes *Trp53inp1*, *Ccng1,* and *Phlda3* were increased, and this increase was statistically significant when levels of *Ccng1,* and *Phlda3* were compared between E9.0 controls and mutants (Figure 5C-D). Thus, we conclude that the increased exon skipping in *Mdm2* and *Mdm4* results in increased nuclear P53, and levels of P53 target genes in *Snrpb*$^{ncc+/-}$ embryos, prior to morphological abnormalities. Since P53 activation can lead to increased apoptosis, we postulate that increased P53 activity contributes to apoptosis of *Snrpb*$^{ncc+/-}$ mutant cells.

Reducing levels of P53 does not rescue craniofacial defects in *Snrpb*$^{ncc/+}$ embryos

We next tested if reducing levels of P53 prevents craniofacial malformations in *Snrpb*$^{ncc+/-}$ embryos. We crossed *Trp53*$^{loxP/+}$; *Wnt1-cre2*$^{tg/+}$ mice and *Snrpb*$^{loxP/+}$ mice and collected E10.5 and E17.5 *Snrpb*$^{ncc+/-}$; *P53*$^{ncc+/-}$ double heterozygous embryos for analysis. We found no significant difference in the proportion of *Snrpb*$^{ncc+/}$*; P53*$^{ncc+/-}$ embryos with mild to severe craniofacial

defects (n=4), when compared to *Snrpb*$^{ncc+/-}$ mutants (n=3/3) (Figure S7C-D and not shown). We then generated *Snrpb*$^{ncc+/-}$ with two mutant *Trp53* alleles in their neural crest cells (*Snrpb*$^{ncc+/-}$; *P53*$^{ncc-/-}$) for cartilage and skeletal analysis. E14.5 *Snrpb*$^{ncc+/-}$; *Trp53*$^{ncc-/-}$ mutant embryos (n=2) resembled *Snrpb*$^{ncc+/-}$ mutants found in group 2 (Figure S7E). Similarly, E18.5 *Snrpb*$^{ncc+/-}$; *Trp53*$^{ncc-/-}$ mutant embryos (n=4) were morphologically similar to group 2 *Snrpb*$^{ncc+/-}$ mutants; they had microcephaly, a shorter snout and micrognathia (Figure S7G). Cartilage and skeletal preps revealed reduced ossification of the frontal bone, cleft palate, and asymmetric and abnormal development of the lower jaw (Figure S7F, H-J). We did not find any *Snrpb*$^{ncc+/-}$ embryos with homozygous loss of *Trp53* in their neural crest cells that were severely abnormal. However, we did not recover any living *Snrpb*$^{ncc+/-}$; *Trp53*$^{ncc-/-}$ pups when the matings were allowed to go to term or find any morphologically normal mutants, suggesting that removing both copies of *Trp53* does not rescue craniofacial defects in *Snrpb*$^{ncc+/-}$ embryos.

Genes required for craniofacial development are abnormally spliced in *Snrpb* $^{ncc+/-}$ mutants

To identify additional abnormal splicing events which could explain craniofacial malformations in *Snrpb* $^{ncc+/-}$ embryos, we queried the MGI database to determine if any transcripts with statistically significant DSEs were required for craniofacial development (Bogue *et al.*, 2017). We identified 13 transcripts required for craniofacial development or stem cell development with significant increases in exon skipping (Table 1). Increased exon skipping in 5 of these genes: *Pdpk1, Rere (Atr2), Mcph1, Nf1,* and *Dyrk2,* is predicted to introduce a pretermination codon. The remaining exon skipping events are not predicted to result in PTC but may alter gene expression and/or function. In fact, all except one of these DSEs were in constitutive exons. We then queried our RNAseq dataset to determine if the expression level of these genes was altered in *Snrpb* mutants. We found no significant changes in levels of transcripts with PTC or Non-PTC skipped exons. We then selected 3-transcripts and performed RT-PCR to confirm that the skipped exon events identified in the RNAseq analysis were present in *Snrpb* mutant heads (Figure 6). This analysis revealed presence of transcripts with skipped exons for *Smad2, Pou2f1* and *Rere*, although the percent spliced events for *Smad2* and *Pou2f1* were below 10%. We postulated that abnormal increases in exon skipping in these 13-transcripts, which are required for normal craniofacial development, contribute to craniofacial defects in *Snrpb*$^{ncc/+}$ mutants.

Wild-type levels of *Snrpb* are required for normal expression of *Fgf8, Shh* and *Msx2*

The surface cephalic ectoderm, of which the facial ectoderm zone (FEZ) is a subregion, is essential for integrating proper growth of the craniofacial skeletons and brain and patterning the underlying neural crest (Griffin *et al.,*2013). The severe malformations found in the face and brain of *Snrpb* mutants suggest that the FEZ might not have formed. Therefore, we used *in situ* hybridization to examine expression of *Shh* and *Fgf8,* which are expressed in surface cephalic ectoderm and together help to define the FEZ (Griffin *et al.,*2013). At E9.5 before the FEZ forms, *Shh* was expressed in the ventral-most region of the neural tube, the floor plate, as well as the ventral prosencephalon of control and *Snrpb*$^{ncc+/-}$ embryos (Figure 7A, n=3). At this stage, *Fgf8* was expressed in the mandibular epithelium, the frontonasal prominence, and the midbrain/hindbrain junction of normal and *Snrpb*$^{ncc+/-}$ mutant embryos. However, the expression domain of *Fgf8* was abnormally expanded at these sites (N=4) (Figure 7B). Furthermore, expression of *Msx2*, a downstream target of *Fgf8* in the underlying neural crest cells *(*Griffin *et al.,*2013*)* was also abnormal in E9.5 *Snrpb*$^{ncc+/-}$ embryos. In control embryos (N=6), *Msx2* was expressed in the distal region of pharyngeal arches 1 and 2 (Figure 7C). However, in *Snrpb*$^{ncc+/-}$ embryos, (n=2) *Msx2* expression was abnormally extended proximally in these arches (Figure 7C). These *in situ*s revealed that normal levels of *Snrpb* is required in the neural crest cells to restrict expression of *Fgf8* and its downstream target *Msx2* in the developing head and face.

In E10.5 group 2 *Snrpb*$^{ncc+/-}$ mutant embryos missing the frontonasal prominence, expression of *Shh* was found in the diencephalon and the ventral forebrain (Figure 7D, n= 2). Furthermore, ectopic *Shh* expression was found in the dorsal and ventral optic lens (arrows in Figure 7D). In group 1 mutant embryos, the lateral and medial nasal processes were further apart than in controls but, *Shh* expression was found in the developing mandibular periderm, and bilaterally on the surface ectoderm of the medial nasal prominences (arrows in Fig 7G). In E10.5 wild type embryos, *Fgf8* was expressed on the surface ectoderm of the mandible, the maxillary prominences, and frontonasal prominences. In group 2 *Snrpb*$^{ncc+/-}$ mutant embryos with a hypoplastic frontonasal and maxillary prominences, expression of *Fgf8* was found on the mandibular ectoderm and in the region where the maxillary prominence would normally form (Figure 7E). In group 1 E10.5 *Snrpb*$^{ncc+/-}$ embryos, *Fgf8* expression in the lateral nasal prominence was reduced, while ectopic expression of *Fgf8* was found on the surface ectoderm of the medial nasal process, towards the midline (Figure 7H). Similarly, in E10.5 group 2 *Snrpb*$^{ncc+/-}$ mutants missing the frontonasal and maxillary prominences, *Msx2* expression was expressed in the

maxillary and in the mandibular region of the hypoplastic first arch. In group 1 *Snrpb*$^{ncc+/-}$ mutants, *Msx2* was expressed in the lateral and medial nasal prominences, although expression appeared reduced but ventrally expanded in the medial frontal nasal region (Figure 7F). Thus, in *Snrpb*$^{ncc+/-}$ embryos where the lateral and medial nasal prominences formed, reduced expression of *Fgf8* in the ectoderm results in abnormal expression of *Msx2* in the underlying neural crest. We postulate that the additive effect of DSEs in genes important for midface development that we found in morphologically normal E9.5 *Snrpb*$^{ncc+/-}$ embryos lead to abnormal expression of *Shh, Fgf8* and *Msx2* expression and mis-patterning of the developing craniofacial region.

DISCUSSION

Splicing is an essential and ubiquitous process that generates mature mRNAs and increases the number and diversity of proteins from the genome (Chen and Manley, 2009; Nilsen and Graveley, 2010). SNRPB is an essential protein that facilitates assembly of the snRNPs proteins that carry out splicing. Surprisingly, mutations that increase levels of a non-functional *SNRPB* transcript result in CCMS, a craniofacial spliceosomopathy that is also associated with rib defects (Lynch *et al*., 2014; Barcot *et al*., 2015 and Beauchamp et al., 2020). To examine the role of *SNRPB* in the development of tissues affected in patients, we first designed guide RNAs and repair templates to generate a mutation in alternative exon 2 that would model those found in CCMS patients (data not shown). However, this strategy did not prove to be fruitful as we did not recover mutant mouse lines carrying this mutation (data not shown). Therefore, we generated a conditional mutant mouse line to test if wild-type levels of *Snrpb* were required for normal development. Herein, we showed that *Snrpb* is haploinsufficient in mice and required for normal splicing of key regulators of P53 and transcripts required for normal craniofacial development. We show that morphological defects in *Snrpb* mutants were not associated with significant changes in gene expression but with alternative splicing suggesting that altered transcript ratios are responsible for defects and embryonic death of mutant embryos.

In our conditional mutant mouse line, deletion of exon 2, alternative exon 2 and exon 3 in the presence of Cre is predicted to generate a shorter *Snrpb* transcript of 527 bp that encodes for a non-functional protein. When *β-actin Cre* was used to delete the *loxP*-flanked exons, the resulting *Snrpb* heterozygous embryos died post-implantation. Therefore, we were unable to study the role of SNRPB in head and rib development in these mutants. Though further studies are needed to

determine if there is a general growth defect or other roles for *Snrpb* at these early stages of development, our study indicates that heterozygosity for a loss of function allele of *Snrpb* is lethal. In fact, a single patient carrying a mutation in the 5' UTR of *SNRPB* that was predicted to result in a null allele was more severely affected and failed to survive gestation (Lynch *et al.*, 2014). Thus, our data support the hypothesis that *SNRPB* mutations commonly found in CCMS patients are not null mutations (Lynch *et al.*, 2014).

To study the role of SNRPB in craniofacial development we used the *Wnt1-Cre2* transgenic mouse line to generate embryos with heterozygous mutation of *Snrpb* in their neural tube and neural crest cells. In *Snrpb*$^{ncc+/-}$ mutant embryos, craniofacial structures derived from neural crest cells, such as the nasal bone, palates, maxilla, mandible, and middle ear structures, are abnormally formed. Intriguingly, these structures are also commonly reported to be affected in CCMS patients, suggesting that abnormal neural crest cell survival and/or differentiation are responsible for defects in those patients. We also uncovered an absence or reduction of the hyoid bone and ectopic cartilages and bones that we could not identify in some *Snrpb*$^{ncc+/-}$ mutants. Similarly, accessory ossicles in the hyoid bone were found after CT scan of two CCMS patients by Tooley *et al.*, 2016. We postulate that SNRPB is required in all neural crest cells, and their derivatives, a fact that is supported by the reduced or absent aorticopulmonary septum that is found in the microCT scan of *Snrpb*$^{ncc+/-}$ mutants. Furthermore, we propose that aorticopulmonary septal defects contribute to death of *Snrpb*$^{ncc+/-}$ embryos, as was found in *Eftud2*$^{ncc-/-}$ mutants (Beauchamp *et al*., 2021). Finally, although phenotypes found in CCMS patients strongly suggested a requirement of SNRPB for endochondral ossification, our data show abnormal development of bones formed via both endochondral and intramembranous ossification, indicating an early role for SNRPB in skeletal development.

P53 stability and activity are known to be upregulated in response to mutation or disruption in the level of splicing factors (Alstyne *et al*., 2018, Correa *et al*. and 2016, Lei *et al.* 2020). In fact, we found increased skipping in two P53-regulators, *Mdm2* exon 3 and *Mdm4* exon 7, increased nuclear P53 and upregulation of P53 target genes in heads of E9.0 *Snrpb*$^{ncc+/-}$ mutants. In zebrafish and mouse, increased P53-activity contributes to craniofacial defects and knocking down or removing P53 genetically reduced apoptosis and improved development (Li L. *et al*., 2017; Mao H. *et al*., 2016). Additionally, we showed that the P53-inhibitor, Pifithrin-α, improved head and brain development in embryos with mutation of *Eftud2* in the neural tube and neural crest

(Beauchamp *et al*., 2021). However, reducing or removing P53 genetically in the neural crest cells did not show rescue of craniofacial defects in *Snrpb*$^{ncc+/-}$ mutant embryos. Although the variable expressivity found in *Snrpb*$^{ncc+/-}$ embryos, makes it difficult to rule out a partial rescue, our findings indicate that P53 alone is probably not responsible for the malformations we found.

RNAseq is a sensitive method for examining gene expression (Wang, Z. *et al.*, 2009), and our data indicate that reduced expression of SNRPB in mutant neural crest disrupts splicing and expression of genes important for craniofacial development. In fact, our RNAseq analysis using the head of morphologically normal E9.0 *Snrpb*$^{ncc+/-}$ embryos revealed many more DSEs than DEGs. We confirmed differential splicing of the P53 regulators, *Mdm2* and *Mdm4* and identified 13 transcripts important for craniofacial development that were abnormally spliced in *Snrpb*$^{ncc+/-}$ embryos. DSE may perturb gene expression levels, for example with the introduction of pretermination codon, or alter the activity or localization of the resulting gene product. For example, the DSE event associated with exon 3 of *Smad2* is predicted to increase the proportion of transcripts that encodes a much more potent effector of TGFβ/Nodal than the full-length SMAD2. This shorter protein heterodimerizes with SMAD3 to regulate many developmental processes, including growth of the mandible (Dunn *et al*., 2005). Similarly, increased skipping of exon 8 of *Ror2* may disrupt the ability of this receptor to interact with *Wnt5* during midface, ear, and jaw development (Schwabe, G.C. *et al.*, 2004). Furthermore, deletions of constitutive exons may change the open reading frame, insert a pretermination codon, or generate an unstable transcript that is removed by nonsense-mediated decay. Hence, we predict that an increase in the proportion of transcripts with a missing constitutive exon will reduce levels of the associated proteins. A consequence of these additive effects likely explains abnormal expression of *Fgf8* which is regulated by SMAD2 (Liu *et al.*, 2004) and *Rere* (Kumar and Duester, 2014). Nonetheless, reduced migration of neural crest cells into the frontonasal region could also explain abnormal expression of *Fgf8* and *Shh.* Though we found no significant differences in the number of neural crest cells in heads of E9.0 control and *Snrpb* mutant embryos, reduced levels of *Nisch*, which binds to integrins to block cell migration (Ding *et al.*, 2008), may disrupt migration of a specific subset of neural crest cells that cannot be identified with our current techniques. In the future, we will investigate contribution of DSEs to abnormal expression of *Fgf8* and *Shh* and to craniofacial defects in *Snrpb* mutants.

Our working model is that dysregulation in the level of SNRPB, even if modest - as is likely the case with inclusion of the PTC containing alternative exon 2, perturbs the efficiency of splicing at the level of spliceosome assembly. Furthermore, although cells with reduced levels of *Snrpb* have an increased propensity to undergo apoptosis, increased DSE is found before they die. Therefore, we propose that splicing changes in important developmental genes, the proportion of cells that undergo apoptosis, and the timing of apoptosis all contribute to the variable expressivity found in *Snrpb* heterozygous mice and in CCMS patients. In conclusion, we believe that our work using the first CCMS animal model shows evidence for both ubiquitous and development-specific roles of *Snrpb* during morphogenesis and provides much needed insights into the role of this splicing factor during embryogenesis.

STAR METHODS

Resource Availability

Lead contact

Further information and requests for resources and reagents should be directed to and will be fulfilled by the Lead Contact, Loydie A. Jerome-Majewska (loydie.majewska@mcgill.ca).

Materials Availability

All antibodies, chemicals and most mouse lines used in this study are commercially available. All other unique materials are available upon request.

Data and code availability

Accession IDs provided by GEO: GSE180546, GSM5464627, GSM5464628, GSM5464629, GSM5464630, GSM5464631, GSM5464632

METHOD DETAILS

Mouse lines

All procedures and experiments were performed according to the guidelines of the Canadian Council on Animal Care and approved by the animal Care Committee of the Montreal Children's Hospital. Wild-type CD1, mT/mG *Gt(ROSA)26Sor*$^{tm4(ACTB\text{-}tdTomato,\text{-}EGFP)Luo}$*/J* , (Soriano, 1999), *Wnt1-Cre2* (Lewis *et.al, 2013),* and *β-actin-cre* (Lewandowski and Martin, 1997) mice on the C57BL/6J genetic background were purchased from The Jackson Laboratory. The *R26R* strain (*Gt (ROSA)26Sor*^{tm1Sor} (Mazumdar et al., 2007) on the mix C57BL/6J;129/S4 genetic background was a kind gift from Dr. Nagano. All strains were maintained on the CD1 genetic background.

Generation and establishment of *Snrpb* conditional mutant mouse lines

To develop a conditional knock-out *Snrpb* allele, we used CRISPR/Cas9-mediated homology-directed repair (HDR) strategy to insert *loxP* sequences in intron 1 and intron 3 to flank exons 2 and 3. Candidate efficient guide RNAs were selected based on previous references (Xu et. al., 2015). Microinjection with single-strand DNA template, guide RNAs, and Cas9 mRNA was done. In the first round of microinjection targeting intron 1, a *loxP* sequence was inserted in intron 1 of 25% of the animals born. The insertion was confirmed in two animals (1 male and 1 female) by Sanger sequencing. We generated homozygous animals with *loxP* sequences in intron 1 from those mice. Intron 1 homozygous *loxP* animals were then used for the second round of microinjection to insert *loxP* in intron 3. Sanger sequencing of DNA from a G1 male offspring of a targeted founder from the second round of microinjection and a wild-type CD1 female was used to confirm that both *loxP* sequences in intron 1 and intron 3 were intact. Thereafter, we backcrossed the animals for at least 5 generations to establish the *Snrpb* conditional mutant mouse line and to remove any potential off-target effect from CRISPR editing. All embryo analysis was of embryos on the mix CD1; C57BL/6J genetic background.

Generation of *Snrpb* $^{+/-}$ mutant embryos

Snrpb $^{+/-}$ mutants were generated by crossing *Snrpb*$^{loxp/+}$ mice with beta actin-Cre $^{tg/+}$ mice.

Generation neural crest cell-specific *Snrpb* $^{+/-}$ mutants

To generate embryos and animals with neural crest-specific *Snrpb* heterozygosity, *Wnt1-Cre2* $^{tg/+}$ animals were mated with *Snrpb* $^{loxp/+}$ mice. Embryos obtained from these matings were *Snrpb* heterozygous mutant in the neural crest cells and their derivatives, while all other cells were *Snrpb* wild type.

Genotyping of mice and embryos

Genomic DNA was extracted from mouse tails or yolk sacs by alkaline lysis (Hou, Gupta *et al*., 2017). For *Snrpb*, genotyping was performed to identify the wild-type and conditional allele (with *loxP* sequences) to amplify segments of intron 1 using the following program: 30 sec 95°C, 30 sec 62°C, 30 sec 72°C for 35 cycles followed by an elongation step of 10 minutes at 72°C. This PCR amplified the targeted DNA segment to determine a wild-type (347 bp) and a mutant (387 bp) amplicon. The primers used for the genotyping were: forward- 5' CCCGAGACAGACACAACATAAG 3', reverse- 5' GCTTTGAAGGTCCCGATGAA 3'. For the commercially available lines, namely R26R, *Wnt1-Cre2*, mT/mG and beta-actin cre genotyping was performed as detailed on Jackson`s laboratory website: protocol# 29915 (*R26R*), #25394 (*Wnt1-Cre2*), #20368 (mT/mG) and ##33618 (beta-actin cre), respectively.

Collection of embryos

The day of plug was considered embryonic day 0.5 (E0.5). On the day of dissection embryos were dissected from their extraembryonic membranes. Yolk sacs were used for genomic DNA extraction and genotyping. All embryos were assessed for the presence of a heartbeat and somite number was counted between E8.5 and E10.5. Embryos were fixed in 4% paraformaldehyde in PBS at 4°C overnight (unless otherwise stated), washed and kept in PBS at 4°C until use.

Wholemount in situ hybridization and preparation of embryos for embedding

Fixed embryos were dehydrated using a graded methanol series for wholemounts. Wholemount RNA *in* situ hybridization was performed as previously described (Revil and Jerome-Majewska 2013). For cryo-embedding, fixed embryos were first cryoprotected in 30% sucrose overnight, embedded in Cryomatrix and stored at -80°C until sectioning.

Cartilage staining of embryos and skeletal preparation of embryos and pups

To investigate cartilage formation, embryos were stained with Alcian Blue (Regeur, 2013). For skeletal staining, the skin was removed from freshly dissected E17.5 embryos and neonatal pups and stained as described by Wallin *et al* . (1994)

Wholemount X-galactosidase staining of embryos

Embryos were stained with freshly prepared X-gal staining solution overnight at 37°C in the dark as described in Beauchamp *et al*, 2021 Post-staining, embryos were embedded in Cryomatrix and stored at -80°C until sectioning. Image J was used to quantify the lacz stained area.

PTA staining for CT scan

Embryos were fixed overnight in 4% PFA and then washed with PBS. After a series of dehydration according to the protocol describe previously (Lesciotto *et al.*, 2020) embryos were stained in 0.7% Phosphotungstic Acid (PTA). The duration of staining varied depending on the stage of the embryos and pre-scanning was done to confirm complete penetration of the PTA. Once all the structures were visualised in the pre-scan, embryos were rehydrated in a series of methanol and CT scanning was done at 20-micrometer thickness.

Immunofluorescence and TUNEL assay

Immunofluorescence experiments were performed on 10-micron thick sections according to standard protocols (Zakariyah et al., 2011). The following primary antibodies were used: Phosphohistone H3 (Ser10) [source] (1:200 dilution). Alexa Fluor 568 [source] (1:500 dilutions) secondary antibody was used. For the quantification of apoptosis, TUNNEL assay was performed according to the manufacturer`s protocol for the cell death detection kit. For quantification of fluorescence signal, particle analysis on Image J was used.

Immunohistochemistry

Embryos were sectioned at 10-micron thickness for immunohistochemistry as previously described (Beauchamp *et al.*,2021; Hou *et al*, 2017). P53 primary antibody (Cell signaling, Cat#2524) was used (1:250 dilution) and the VECTASTAIN® Universal Quick HRP Kit was used as secondary antibody and visualized with DAB.

RNA isolation for RNA sequencing

RNA extraction was done using Qiagen RNeasy kit following manufacturer's protocol from samples stored in RNA later (Invitrogen). For RNA isolation at E9.0, heads of two somite-matched embryos from different litters were pooled according to genotype. 3 wild-type and heterozygous pools were used for RNA sequencing analysis.

qRT-PCR

Total RNA was treated with DNAse (NEB, according to manufacturer's protocol) and used for reverse transcription with the iScript™ Reverse Transcription Supermix for RT. qRT-PCR was performed using the Advanced universal SYBR® Green Supermix. RT-qPCR experiments were performed in duplicates to ensure technical replicability. Target genes were normalized with the normalization factor as calculated by geNorm software (Vandesompele *et al*. 2002). Three house-keeping genes including B2M, GAPDH, and SDHA were used for generation of the normalization factor as previously reported (Vandesompele *et al*. 2002).

RNA sequencing Analysis

Sequencing libraries were prepared by McGill Genome Centre (Montreal, Canada), using the TruSeq Stranded Total RNA Sample Preparation Kit (Illumina TS-122-2301, San Diego, California, United States) by depleting ribosomal and fragmented RNA, synthesizing first and second strand cDNA, adenylating the 3′ ends and ligating adaptors, and enriching the adaptor-containing cDNA strands by PCR. The libraries were sequenced using the Illumina NovaSeq 6000 PE100 sequencer, 100 nucleotide paired-end reads, generating between 109 and 230 million reads sample. The sequencing reads were trimmed using CutAdapt (Martin M., 2011) and mapped to the mouse reference genome (mm10) using STAR (Dobin A et al., 2013) aligner (version 2.6.1d), with default parameters, and annotated using the Gencode (Harrow J *et al.*, 2006) M2 (version M2, 2013) annotation. htseq-count (part of the 'HTSeq' (Anders S *et al.*, 2015) framework, version 0.13. 5) was used for expression quantification.

To perform a differential splicing analysis, rMATS 4.0.2 (Shen S. *et al.*, 2014) was used and detected splicing events were filtered by systematically excluding those with a mean of inclusion junction counts (IJC) lower than 5 in either wild-type or heterozygous samples. To identify significant DSE, an absolute inclusion level difference (ILD) cut-off of more than 0.05 was used and a Benjamin-Hochberg multiple testing correction with a False Discovery Rate (FDR) cut-off of less than 0.1 was used. The rationale for relaxing the FDR cut-off here was to obtain a large dataset enriched for alternative splicing events in order to observe general tendencies, such as increased propensity for exon skipping or intron retention in the mutants. To characterize 3'SS

sequences, LaBranchoR (Paggi and Bejerano, 2018), a branchpoint (BP) prediction tool based on a deep-learning approach was used, that uses a bidirectional long short-term memory network (LSTM) model, to identify relevant branchpoints upstream DSEs. The BPs and their surrounding area consensus motifs were generated using WebLogo 3.0 (Crooks GE *et al.*,2004).

For differential expression analysis (DEA), we used DESeq2 (Love M.I. e*t al.*, 2014) package and a list of significant DEG was derived using a FDR cut-off of less than 0.05 with no additional restriction on the absolute log2 fold change (Log2FC) (to allow for detection of even minor expression changes). For KEGG pathway analyses, the combined list of up- and down-regulated genes from DEA was used as input to gProfiler2 (Raudvere U. et al., 2019) package (gost function), and all the detected genes from DEA were used as background.

A differential analysis of transposable element (TE) and lncRNA expression was also carried out, to investigate whether SNRPB deficiency may result in deregulation of the non-coding transcriptome. Those analyses did not uncover any differences in the mutant embryos, and the results are not shown in the manuscript. STAR was used to map the processed reads with modified options:—outFilterMultimapNmax 100 —winAnchorMultimapNmax 100 —outMultimapperOrder Random —alignSJoverhangMin 8 —outFilterMismatchNmax 999 —alignIntronMin 20 —alignIntronMax 1000000 —alignMatesGapMax 1000000, with mouse annotations to guide mapping, coming from the UCSC repeat masker (Gencode M1) and lncRNA (Gencode M1) annotations. The mapped lncRNA and TE reads were respectively quantified with salmon (Patro R. *et al.*, 2017) and TElocal (Jin Y *et al.*, 2014). Differential lncRNA and TE expression analysis were performed using DESeq2, with the TE and lncRNA read counts being normalized using protein-coding gene expression size factors and differentially expressed lncRNA and TE selected based on a FDR cut-off of less than 0.05 and an absolute Log2FC of greater than 0.5 to increase detection signal.

Quantification and Statistical analysis

Quantitation was performed using Image J software (NIH). Statistical analyses were conducted using GraphPad Prism 8.0 software (GraphPad Prism, San Diego, CA, USA). Two-tailed unpaired Man Whitney t-test analysis was calculated Prism Software and Chi-square test was also calculated using Prism. Significant p-values are represented as *P<0.05, **P<0.01 and ***P<0.001.

ACKNOWLEDGEMENT

We would like to thank Dr. Mitra Cowan, Platform Manager, McGill Integrated Core of Animal Modeling (MICAM) for performing the microinjection experiments. This project was funded in parts by Canadian Institutes of Health Research (CIHR) and bridge funding from the Research Institute of McGill University Health Centre (RI-MUHC). We also thank Queen Elizabeth Scholars (QES) Program, Research Institute of McGill University Health Centre (RI-MUHC) and McGill Faculty of Medicine and Health Sciences for supporting Sabrina Alam. The funders had no role in study design, data collection and analyses, decision to publish or preparation of the manuscript. We acknowledge the professional and technical support from the Animal Resource Division (ARD) of RI-MUHC for maintaining our mice colonies. We are also thankful to the Small Animal Imaging Labs, Centre for Translational Biology, RI-MUHC for their support in performing the microCT scans. LJM and JM are members of the Research Centre of the McGill University Health Centre which is funded in parts by FRQS.

AUTHOR CONTRIBUTIONS

L.J.M. and J.M. conceptualized and supervised the project; E.B., R.P. and S.J.Z. analyzed all the RNA sequencing data, S.K. performed RT-qPCR experiments and analyses; M.C.B performed 2H3 immunostaining, P53 immunohistochemistry, and in situ experiments and analysis, A.B. performed proliferation and apoptosis analysis; N.N. performed skeletal preparation analysis, S.S.A. performed all other experiments done in the study; L.J.M., J.M, and S.S.A wrote the manuscript with inputs from all authors.

DECLARATION OF INTERESTS

The authors declare no competing interests

References:

Anders S, Pyl PT, Huber W. 2015. HTSeq--a Python framework to work with high-throughput sequencing data. Bioinformatics 31: 166-169.

Bacrot S, Doyard M, Huber C, Alibeu O, Feldhahn N, Lehalle D, Lacombe D, Marlin S, Nitschke P, Petit F et al. 2015. Mutations in SNRPB, encoding components of the core splicing machinery, cause cerebro-costo-mandibular syndrome. Hum Mutat 36: 187-190.

Beauchamp MC, Alam SS, Kumar S, Jerome-Majewska LA. 2020. Spliceosomopathies and neurocristopathies: Two sides of the same coin? Dev Dyn 249: 924-945.

Beauchamp MC, Djedid A, Bareke E, Merkuri F, Aber R, Tam AS, Lines MA, Boycott KM, Stirling PC, Fish JL et al. 2021. Mutation in Eftud2 causes craniofacial defects in mice via mis-splicing of Mdm2 and increased P53. Hum Mol Genet 30: 739-757.

Bogue MA, Grubb SC, Walton DO, Philip VM, Kolishovski G, Stearns T, Dunn MH, Skelly DA, Kadakkuzha B, TeHennepe G et al. 2017. Mouse Phenome Database: an integrative database and analysis suite for curated empirical phenotype data from laboratory mice. Nucleic Acids Research 46: D843-D850.

Brannan CI, Perkins AS, Vogel KS, Ratner N, Nordlund ML, Reid SW, Buchberg AM, Jenkins NA, Parada LF, Copeland NG. 1994. Targeted disruption of the neurofibromatosis type-1 gene leads to developmental abnormalities in heart and various neural crest-derived tissues. Genes Dev 8: 1019-1029.

Chen M, Manley JL. 2009. Mechanisms of alternative splicing regulation: insights from molecular and genomics approaches. Nat Rev Mol Cell Biol 10: 741-754.

Correa BR, de Araujo PR, Qiao M, Burns SC, Chen C, Schlegel R, Agarwal S, Galante PA, Penalva LO. 2016. Functional genomics analyses of RNA-binding proteins reveal the splicing regulator SNRPB as an oncogenic candidate in glioblastoma. Genome Biol 17: 125.

Crompton M, Purnell T, Tyrer HE, Parker A, Ball G, Hardisty-Hughes RE, Gale R, Williams D, Dean CH, Simon MM et al. 2017. A mutation in Nischarin causes otitis media via LIMK1 and NF-kappaB pathways. PLoS Genet 13: e1006969.

Crooks GE, Hon G, Chandonia JM, Brenner SE. 2004. WebLogo: a sequence logo generator. Genome Res 14: 1188-1190.

Ding Y, Milosavljevic T, Alahari SK. 2008. Nischarin inhibits LIM kinase to regulate cofilin phosphorylation and cell invasion. Mol Cell Biol 28: 3742-3756.

Dobin A, Davis CA, Schlesinger F, Drenkow J, Zaleski C, Jha S, Batut P, Chaisson M, Gingeras TR. 2013. STAR: ultrafast universal RNA-seq aligner. Bioinformatics 29: 15-21.

Donner AL, Episkopou V, Maas RL. 2007. Sox2 and Pou2f1 interact to control lens and olfactory placode development. Dev Biol 303: 784-799.

Dunn NR, Koonce CH, Anderson DC, Islam A, Bikoff EK, Robertson EJ. 2005. Mice exclusively expressing the short isoform of Smad2 develop normally and are viable and fertile. Genes Dev 19: 152-163.

Fregeau B, Kim BJ, Hernandez-Garcia A, Jordan VK, Cho MT, Schnur RE, Monaghan KG, Juusola J, Rosenfeld JA, Bhoj E et al. 2016. De Novo Mutations of RERE Cause a

Genetic Syndrome with Features that Overlap Those Associated with Proximal 1p36 Deletions. Am J Hum Genet 98: 963-970.
Griffin JN, Compagnucci C, Hu D, Fish J, Klein O, Marcucio R, Depew MJ. 2013. Fgf8 dosage determines midfacial integration and polarity within the nasal and optic capsules. Dev Biol 374: 185-197.
Gruber R, Zhou Z, Sukchev M, Joerss T, Frappart PO, Wang ZQ. 2011. MCPH1 regulates the neuroprogenitor division mode by coupling the centrosomal cycle with mitotic entry through the Chk1-Cdc25 pathway. Nat Cell Biol 13: 1325-1334.
Harrow J, Denoeud F, Frankish A, Reymond A, Chen CK, Chrast J, Lagarde J, Gilbert JG, Storey R, Swarbreck D et al. 2006. GENCODE: producing a reference annotation for ENCODE. Genome Biol 7 Suppl 1: S4 1-9.
Hou W, Gupta S, Beauchamp MC, Yuan L, Jerome-Majewska LA. 2017. Non-alcoholic fatty liver disease in mice with heterozygous mutation in TMED2. PLoS One 12: e0182995.
Hwang JY, Jung S, Kook TL, Rouchka EC, Bok J, Park JW. 2020. rMAPS2: an update of the RNA map analysis and plotting server for alternative splicing regulation. Nucleic Acids Res 48: W300-W306.
Jin Y, Tam OH, Paniagua E, Hammell M. 2015. TEtranscripts: a package for including transposable elements in differential expression analysis of RNA-seq datasets. Bioinformatics 31: 3593-3599.
Jones NC, Lynn ML, Gaudenz K, Sakai D, Aoto K, Rey JP, Glynn EF, Ellington L, Du C, Dixon J et al. 2008. Prevention of the neurocristopathy Treacher Collins syndrome through inhibition of p53 function. Nat Med 14: 125-133.
Kumar S, Duester G. 2014. Retinoic acid controls body axis extension by directly repressing Fgf8 transcription. Development 141: 2972-2977.
Lawlor MA, Mora A, Ashby PR, Williams MR, Murray-Tait V, Malone L, Prescott AR, Lucocq JM, Alessi DR. 2002. Essential role of PDK1 in regulating cell size and development in mice. EMBO J 21: 3728-3738.
Lei L, Yan SY, Yang R, Chen JY, Li Y, Bu Y, Chang N, Zhou Q, Zhu X, Li CY et al. 2017. Spliceosomal protein eftud2 mutation leads to p53-dependent apoptosis in zebrafish neural progenitors. Nucleic Acids Res 45: 3422-3436.
Lesciotto KM, Motch Perrine SM, Kawasaki M, Stecko T, Ryan TM, Kawasaki K, Richtsmeier JT. 2020. Phosphotungstic acid-enhanced microCT: Optimized protocols for embryonic and early postnatal mice. Dev Dyn 249: 573-585.
Lewandoski M, Meyers EN, Martin GR. 1997. Analysis of Fgf8 gene function in vertebrate development. Cold Spring Harb Symp Quant Biol 62: 159-168.
Lewis AE, Vasudevan HN, O'Neill AK, Soriano P, Bush JO. 2013. The widely used Wnt1-Cre transgene causes developmental phenotypes by ectopic activation of Wnt signaling. Dev Biol 379: 229-234.
-. 2013. The widely used Wnt1-Cre transgene causes developmental phenotypes by ectopic activation of Wnt signaling. Dev Biol 379: 229-234.

Liu Y, Festing M, Thompson JC, Hester M, Rankin S, El-Hodiri HM, Zorn AM, Weinstein M. 2004. Smad2 and Smad3 coordinately regulate craniofacial and endodermal development. Dev Biol 270: 411-426.
Love MI, Huber W, Anders S. 2014. Moderated estimation of fold change and dispersion for RNA-seq data with DESeq2. Genome Biol 15: 550.
Lynch DC, Revil T, Schwartzentruber J, Bhoj EJ, Innes AM, Lamont RE, Lemire EG, Chodirker BN, Taylor JP, Zackai EH et al. 2014. Disrupted auto-regulation of the spliceosomal gene SNRPB causes cerebro-costo-mandibular syndrome. Nat Commun 5: 4483.
Mao H, McMahon JJ, Tsai YH, Wang Z, Silver DL. 2016. Haploinsufficiency for Core Exon Junction Complex Components Disrupts Embryonic Neurogenesis and Causes p53-Mediated Microcephaly. PLoS Genet 12: e1006282.
Muzumdar MD, Tasic B, Miyamichi K, Li L, Luo L. 2007. A global double-fluorescent Cre reporter mouse. Genesis 45: 593-605.
Nilsen TW, Graveley BR. 2010. Expansion of the eukaryotic proteome by alternative splicing. Nature 463: 457-463.
Nomura M, Li E. 1998. Smad2 role in mesoderm formation, left-right patterning and craniofacial development. Nature 393: 786-790.
Olthof AM, Hyatt KC, Kanadia RN. 2019. Minor intron splicing revisited: identification of new minor intron-containing genes and tissue-dependent retention and alternative splicing of minor introns. BMC Genomics 20: 686.
Paggi JM, Bejerano G. 2018. A sequence-based, deep learning model accurately predicts RNA splicing branchpoints. RNA 24: 1647-1658.
Patro R, Duggal G, Love MI, Irizarry RA, Kingsford C. 2017. Salmon provides fast and bias-aware quantification of transcript expression. Nat Methods 14: 417-419.
Raudvere U, Kolberg L, Kuzmin I, Arak T, Adler P, Peterson H, Vilo J. 2019. g:Profiler: a web server for functional enrichment analysis and conversions of gene lists (2019 update). Nucleic Acids Res 47: W191-W198.
Revil T, Jerome-Majewska LA. 2013. During embryogenesis, esrp1 expression is restricted to a subset of epithelial cells and is associated with splicing of a number of developmentally important genes. Dev Dyn 242: 281-290.
Saltzman AL, Pan Q, Blencowe BJ. 2011. Regulation of alternative splicing by the core spliceosomal machinery. Genes Dev 25: 373-384.
Schwabe GC, Trepczik B, Suring K, Brieske N, Tucker AS, Sharpe PT, Minami Y, Mundlos S. 2004. Ror2 knockout mouse as a model for the developmental pathology of autosomal recessive Robinow syndrome. Dev Dyn 229: 400-410.
Scotti M, Kmita M. 2012. Recruitment of 5' Hoxa genes in the allantois is essential for proper extra-embryonic function in placental mammals. Development 139: 731-739.
Shen S, Park JW, Lu ZX, Lin L, Henry MD, Wu YN, Zhou Q, Xing Y. 2014. rMATS: robust and flexible detection of differential alternative splicing from replicate RNA-Seq data. Proc Natl Acad Sci U S A 111: E5593-5601.
Soriano P. 1999. Generalized lacZ expression with the ROSA26 Cre reporter strain. Nat Genet 21: 70-71.

Tooley M, Lynch D, Bernier F, Parboosingh J, Bhoj E, Zackai E, Calder A, Itasaki N, Wakeling E, Scott R et al. 2016. Cerebro-costo-mandibular syndrome: Clinical, radiological, and genetic findings. Am J Med Genet A 170A: 1115-1126.
Van Alstyne M, Simon CM, Sardi SP, Shihabuddin LS, Mentis GZ, Pellizzoni L. 2018. Dysregulation of Mdm2 and Mdm4 alternative splicing underlies motor neuron death in spinal muscular atrophy. Genes Dev 32: 1045-1059.
Vandesompele J, De Preter K, Pattyn F, Poppe B, Van Roy N, De Paepe A, Speleman F. 2002. Accurate normalization of real-time quantitative RT-PCR data by geometric averaging of multiple internal control genes. Genome Biol 3: RESEARCH0034.
Vissers LE, Cox TC, Maga AM, Short KM, Wiradjaja F, Janssen IM, Jehee F, Bertola D, Liu J, Yagnik G et al. 2011. Heterozygous mutations of FREM1 are associated with an increased risk of isolated metopic craniosynostosis in humans and mice. PLoS Genet 7: e1002278.
Wallin J, Wilting J, Koseki H, Fritsch R, Christ B, Balling R. 1994. The role of Pax-1 in axial skeleton development. Development 120: 1109-1121.
Wang Z, Gerstein M, Snyder M. 2009. RNA-Seq: a revolutionary tool for transcriptomics. Nat Rev Genet 10: 57-63.
White JK, Gerdin AK, Karp NA, Ryder E, Buljan M, Bussell JN, Salisbury J, Clare S, Ingham NJ, Podrini C et al. 2013. Genome-wide generation and systematic phenotyping of knockout mice reveals new roles for many genes. Cell 154: 452-464.
Wickramasinghe VO, Gonzalez-Porta M, Perera D, Bartolozzi AR, Sibley CR, Hallegger M, Ule J, Marioni JC, Venkitaraman AR. 2015. Regulation of constitutive and alternative mRNA splicing across the human transcriptome by PRPF8 is determined by 5' splice site strength. Genome Biol 16: 201.
Xu H, Xiao T, Chen CH, Li W, Meyer CA, Wu Q, Wu D, Cong L, Zhang F, Liu JS et al. 2015. Sequence determinants of improved CRISPR sgRNA design. Genome Res 25: 1147-1157.
Yeo G, Burge CB. 2004. Maximum entropy modeling of short sequence motifs with applications to RNA splicing signals. J Comput Biol 11: 377-394.
Yoshida S, Aoki K, Fujiwara K, Nakakura T, Kawamura A, Yamada K, Ono M, Yogosawa S, Yoshida K. 2020. The novel ciliogenesis regulator DYRK2 governs Hedgehog signaling during mouse embryogenesis. Elife 9.
Zakariyah A, Hou W, Slim R, Jerome-Majewska L. 2012. TMED2/p24beta1 is expressed in all gestational stages of human placentas and in choriocarcinoma cell lines. Placenta 33: 214-219.
Zhang J, Yang R, Liu Z, Hou C, Zong W, Zhang A, Sun X, Gao J. 2015. Loss of lysyl oxidase-like 3 causes cleft palate and spinal deformity in mice. Hum Mol Genet 24: 6174-6185.
Zhu L, Zhang X, Sun Z. 2020. SNRPB promotes cervical cancer progression through repressing p53 expression. Biomed Pharmacother 125: 109948.
Zoltewicz JS, Stewart NJ, Leung R, Peterson AS. 2004. Atrophin 2 recruits histone deacetylase and is required for the function of multiple signaling centers during mouse embryogenesis. Development 131: 3-14.

Table 1. Increased SE of craniofacial developmental genes in *Snrpb* $^{ncc+/-}$ mutants. Transcripts required for normal head/craniofacial development with a significant increase in skipped exons are not all predicted to result in PTC in *Snrpb*$^{ncc+/-}$.

Gene name	Skipped Exon	PTC	Phenotype	Constitutive exon
1. Smad2	Exon 3	No	Mandible hypoplasia (Nomura and Li, 1998)	No
2. Loxl3	Exon 2	No	Cleft palate, short and bent mandible (Zhang *et al.*, 2015)	No
3. Ror2	Exon 8	No	Midface hypoplasia, truncated Meckel's, middle ear defect (Schwabe, G.C. *et al.*, 2004)	Yes
4. Nisch	Exon 6	No	Short snout (Crompton, M. *et al.*, 2017)	Yes
5. Pou2f1	Exon 4	No	Abnormal nasal placode development when removed with *Sox2* (Donner, A.L. *et al.*, 2006)	Yes
6. Rgl1	Exon 3	No	Abnormal frontal bone, short snout, abnormal maxilla and mandibular morphology (Mouse Genome Informatics and the International Mouse Phenotyping Consortium, 2014)	Yes
7. Frem1	Exon 32	No	Midface hypoplasia, asymmetry, short snout (Vissers, L.E. *et al.*, 2011)	Yes
8. Smc3	Exon 5	No	Upturned snout (White, J.K. *et al.*, 2013)	Yes
9. Pdpk1	Exon 3	Yes	Abnormalities in the head, nasal cartilage (Lawlor, M.A. *et al.*, 2002)	Yes
10. Rere (*Atr2*)	Exon 4	Yes	Small pharyngeal arch (Zoltewicz, J.S. *et al.*, 2004)	Yes
11. Mcph1	Exon 13	Yes	Microcephaly (Gruber, R. *et al.*, 2011)	Yes
12. Nf1	Exon 56	Yes	Head hyperplasia, aorticopulmonary septal defect, heart defects (Brannan, C.I. *et al.*, 1994)	Yes
13. Dyrk2	Exon 2	Yes	Cleft palate (Yoshida, S. *et al.*, 2020)	No

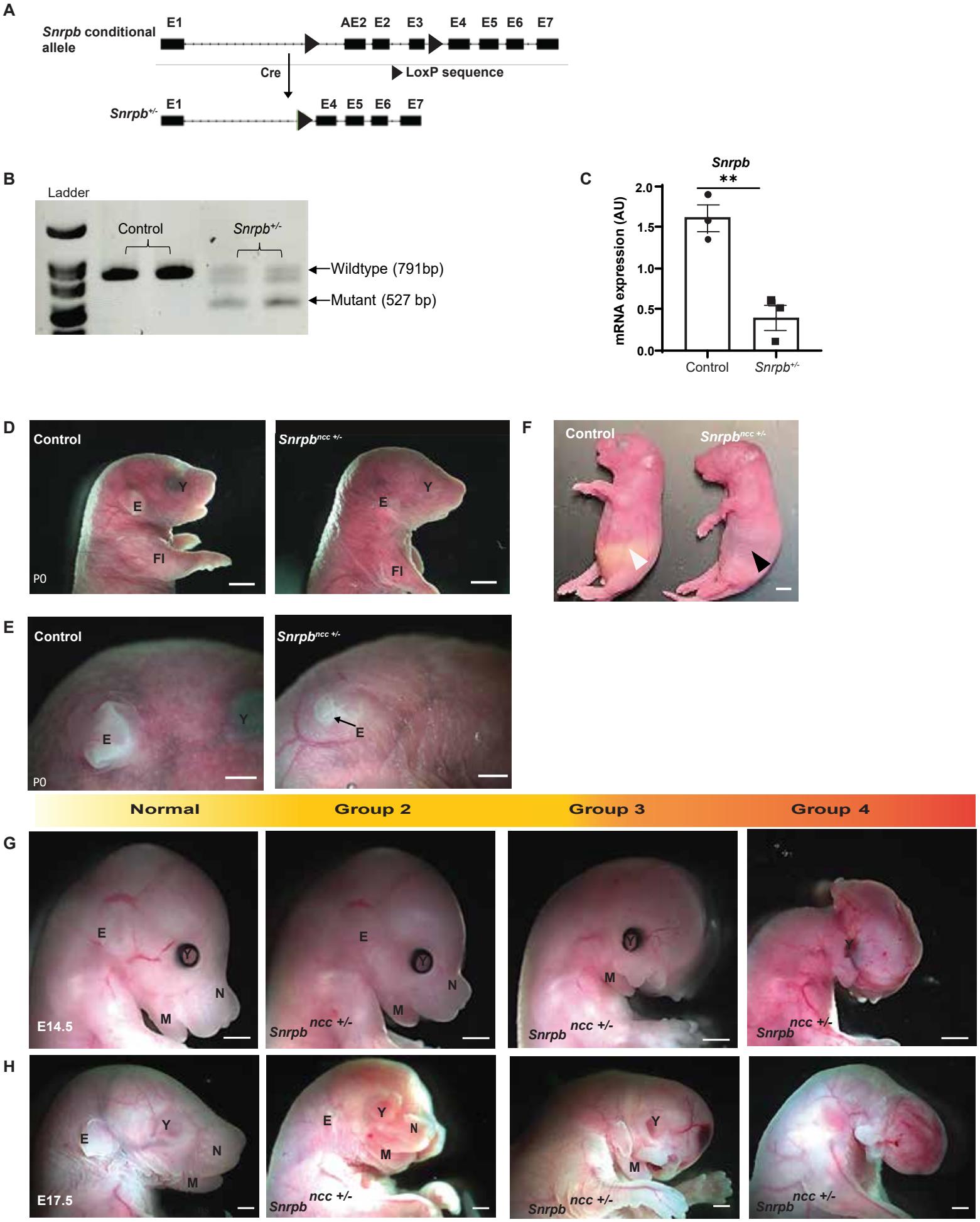
A
Snrpb conditional allele
E1
AE2 E2 E3 E4 E5 E6 E7
Cre
LoxP sequence
Snrpb+/-
E1
E4 E5 E6 E7
B
Ladder
Control
Snrpb+/-
Wildtype (791bp)
Mutant (527 bp)
C
Snrpb
**
mRNA expression (AU)
2.0
1.5
1.0
0.5
0.0
Control
Snrpb+/-
D
Control
Snrpbncc +/-
Y
E
Fl
P0
F
Control
Snrpbncc +/-
E
Control
Snrpbncc +/-
Y
E
P0
Normal
Group 2
Group 3
Group 4
G
E
Y
N
M
E14.5
Snrpb ncc +/-
H
E17.5
Snrpb ncc +/-

Figure 1: Deletion of Exons 2- 3 of *Snrpb* results in reduced *Snrpb* level and craniofacial malformations of varying severity in *Snrpb*$^{Loxp/+}$;*Wnt-1 Cre2*$^{tg/+}$ embryos **A**. Schema of the conditional *Snrpb*$^{LoxP/+}$ allele generated using CRISPR/Cas9 and the deletion generated in the presence of *Cre*. **B**. Deletion of the *LoxP* flanked exons 2 – 3 in *Snrpb* produces a shorter transcript of 527 base-pairs, and reduced levels of this gene in E8.5 in *Snrpb*$^{+/-}$ mutant embryos **C**. RT-qPCR revealed a significant decrease in *Snrpb* level in E8.5 heterozygous mutant embryos. **D**. *Snrpb*$^{Loxp/+}$;*Wnt-1 Cre2*$^{tg/+}$ pups (*Snrpb*$^{ncc+/-}$) found at P0 have an abnormally shaped head, micrognathia and abnormal outer ears. **E**. Higher magnification showing a hypoplastic pinna (E) in the *Snrpb*$^{ncc+/-}$ mutant (black arrow). **F**. *Snrpb*$^{ncc+/-}$ mutant pups lack milk spot in their stomach (black arrowhead), which is visible in the control littermate (white arrowhead). **G-H**. *Snrpb*$^{ncc+/-}$ mutants at E14.5 and E17.5 show a range of craniofacial malformations, Group 2 had abnormal outer ear, cranial and mandibular hypoplasia, Group 3 had nasal clefts, Group 4 showed severe abnormalities including absence of the head and face. E=Ear, N=Nose, Fl=Forelimb, Hf=Headfold, Fb=Forebrain, Mb=Midbrain, Hb=Hindbrain, Ov=Otic vesicle, Ys=Yolk sac, Ht=Heart, Y=Eye, M=Mandible, 1=Pharyngeal arch 1, 2=Pharyngeal arch 2.

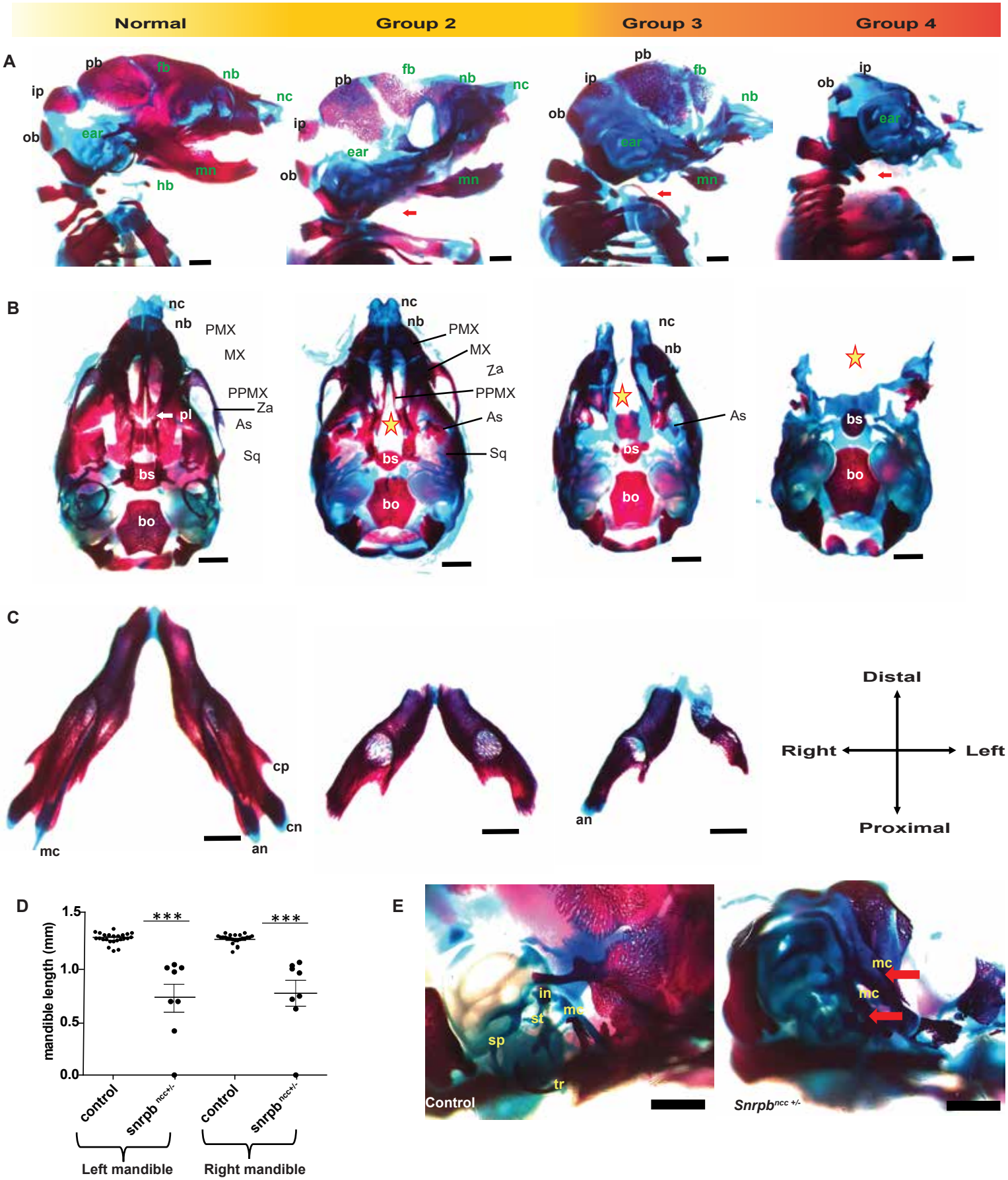
Normal
Group 2
Group 3
Group 4
A
pb
fb
nb
nc
ip
ob
ear
mn
hb
B
nc
nb
PMX
MX
PPMX
Za
pl
As
Sq
bs
bo
C
cp
cn
mc
an
Distal
Right
Left
Proximal
D
mandible length (mm)
1.5
1.0
0.5
0.0
***
***
control
snrpb ncc+/-
control
snrpb ncc+/-
Left mandible
Right mandible
E
in
st
me
sp
tr
Control
mc
mc
Snrpb ncc +/-

Figure 2: Craniofacial cartilages and bones of *Snrpb*$^{ncc+/-}$ embryos are hypoplastic or fail to form. A. Sagittal view of E17.5 mutants showing abnormal formation of craniofacial bones. Neural crest cell derived bones (labeled in green letters) are predominantly affected in *Snrpb*$^{ncc+/-}$ mutants. **B**. Ventral view of the skull showing palatal and maxillary clefts (star) in groups 2 and 3 mutants, respectively, and the absence of the ventral craniofacial components in group 4 mutants. **C**. Asymmetric mandibles and absent condylar and coronoid processes were found in *Snrpb*$^{ncc+/-}$ mutants. **D**. Both left and right mandibles are significantly shorter in *Snrpb*$^{ncc+/-}$ embryos ($p<.0001$, T-test), when compared to controls. **E**. Variable middle ear defects were found. Middle ear structures such as the stapes were absent in some mutants, whereas a presumably duplicated Meckel's cartilage and ectopic structures were found in a subset. nc= nasal cartilage, nb=nasal bone, fb=frontal bone, ob=occipital bone, hb=hyoid bone, mn=mandible, pl=palatine, bo=basioccipital bone, bs=basisphenoid bone, cp=coronoid process, cn=condylar process, an=angle, mc=Meckel's cartilage, ml=melius, in=incus, st=stepes, sp=styloid process, PMX=premaxilla, MX=maxilla, PPMX= palatal process of maxilla, Za=zygomatic arch, As=alisphenoid bone, Sq=squamous bone

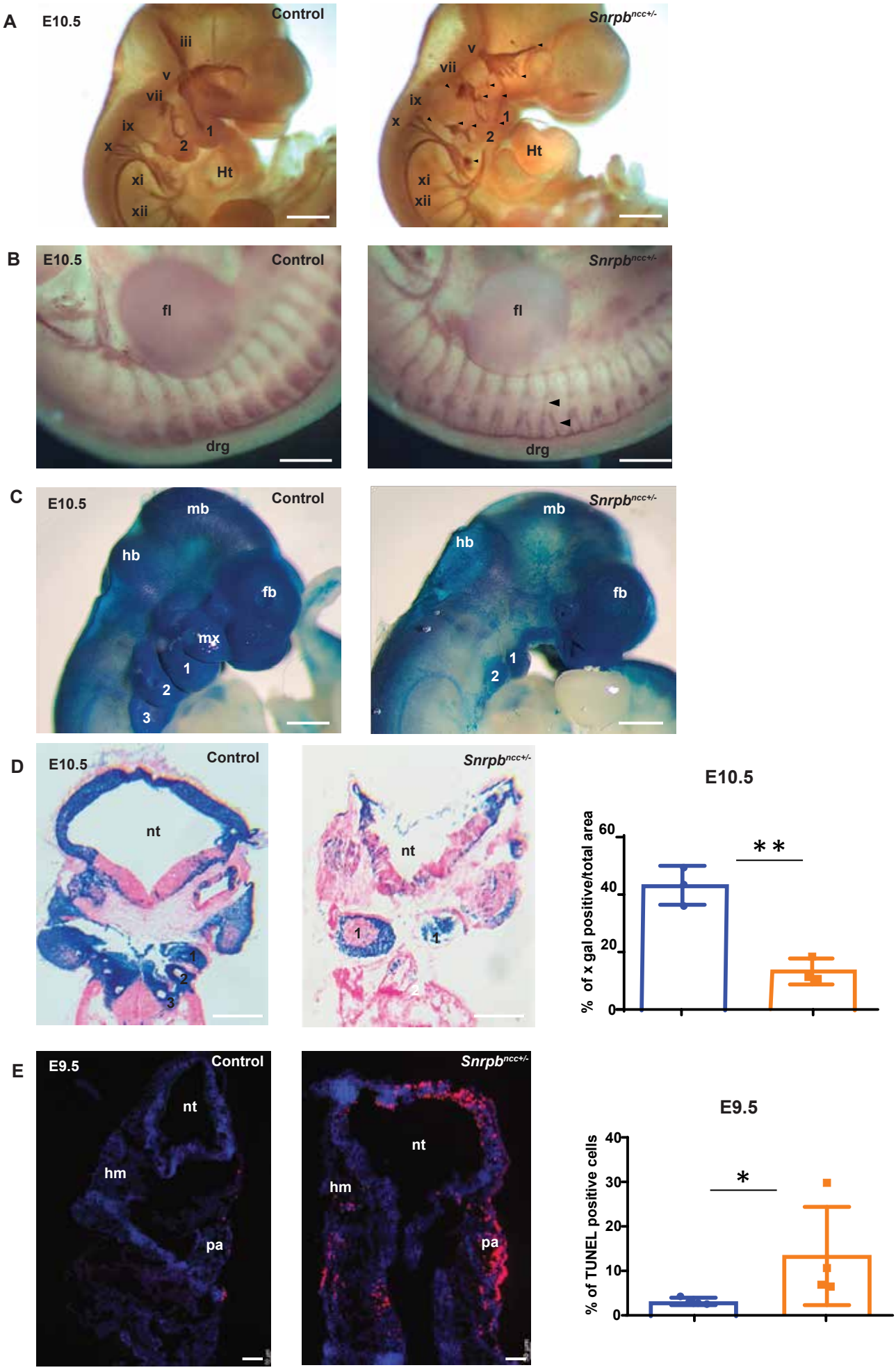
A
E10.5
Control
iii
v
vii
ix
x
1
2
Ht
xi
xii
Snrpb ncc+/-
B
E10.5
Control
fl
drg
Snrpb ncc+/-
C
E10.5
Control
mb
hb
fb
mx
1
2
3
Snrpb ncc+/-
D
E10.5
Control
nt
Snrpb ncc+/-
E10.5
% of x gal positive/total area
60
40
20
0
**
E
E9.5
Control
nt
hm
pa
Snrpb ncc+/-
E9.5
% of TUNEL positive cells
40
30
20
10
0
*

Figure 3: Abnormal cranial ganglia, reduced cranial neural crest cells, and a significant increase in cell death in *Snrpb*$^{ncc+/-}$ mutants. **A**. 2H3 immunostaining showing normal cranial ganglia formation in a control embryo. *Snrpb*$^{ncc+/-}$ mutants (n=2) showed abnormal projections of nerves to the pharyngeal arches (cranial ganglion v and vii) and heart (cranial ganglion ix) and absence and abnormal bundling of cranial nerves (all are shown in black arrowheads). **B**. When compared to the controls, the dorsal root ganglia are bifurcated and reduced in mutants (arrowheads). **C**. Wholemount X-gal staining of E10.5 control and mutant embryos show fewer mutant cells in the craniofacial region and the pharyngeal arches of mutants (n=4) when compared to the control embryos (n=4) **D**. Cryosection of X-gal-stained embryos (n=3) showing a significant reduction in mutant cells when compared to control littermates (T-test, $p<.005$) **E**. The number of TUNEL positive nuclei (red) is significantly increased in E9.5 *Snrpb*$^{ncc+/-}$ mutants (n=3) (T-test, $p<.05$). 1, 2, 3 =pharyngeal arches 1, 2 and 3, drg=dorsal root ganglia, fl=forelimb, hl=hindlimb, fb=forebrain, mb=midbrain, mx=maxillary prominence, hb=hindbrain, hm=head mesenchyme, nt=neural tube, ht=heart

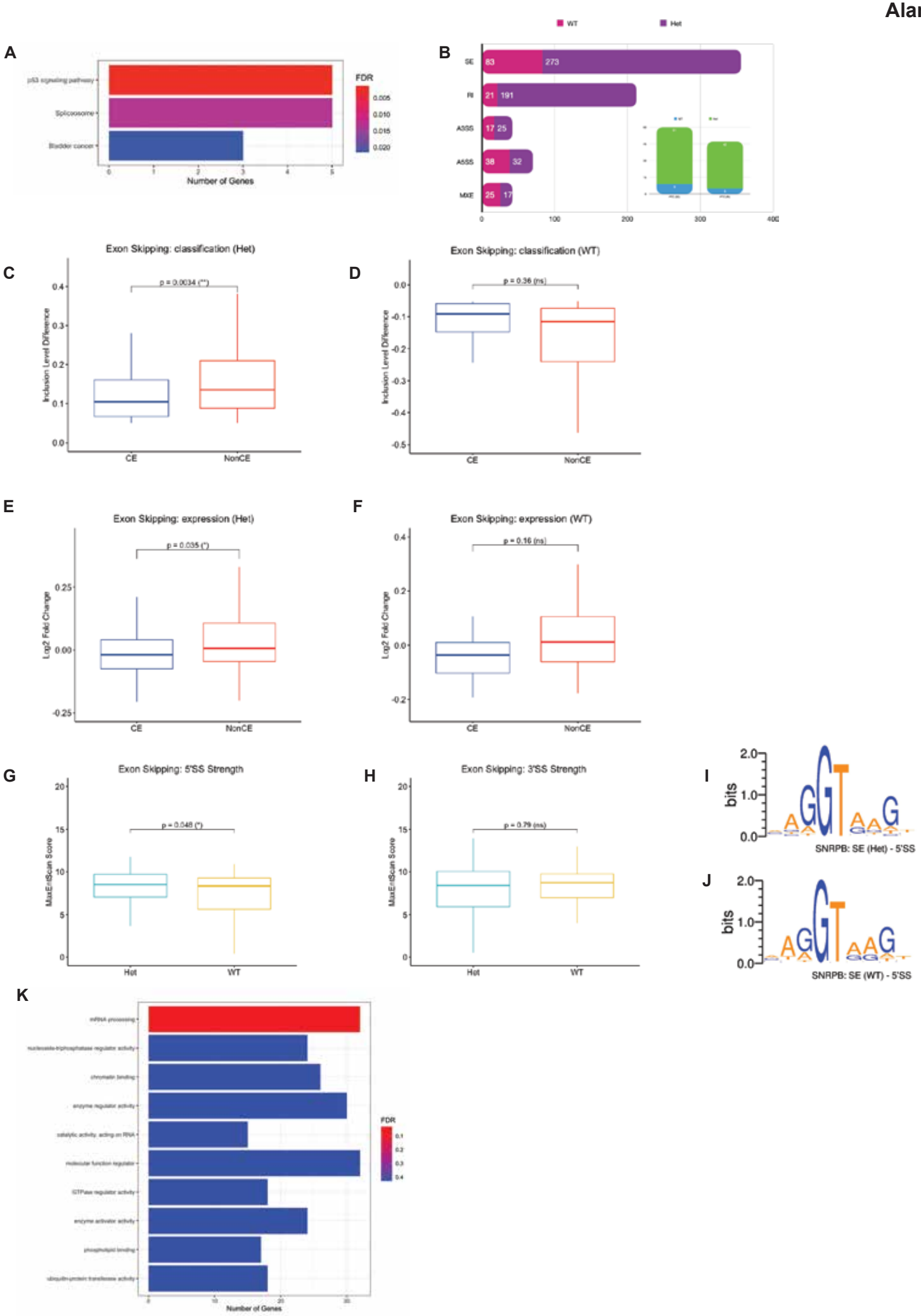
A
p53 signaling pathway
Spliceosome
Bladder cancer
FDR
0.005
0.010
0.015
0.020
Number of Genes
B
WT
Het
SE
RI
A3SS
A5SS
MXE
83
273
21
191
17
25
38
32
25
17
C
Exon Skipping: classification (Het)
p = 0.0034 (**)
Inclusion Level Difference
CE
NonCE
D
Exon Skipping: classification (WT)
p = 0.36 (ns)
Inclusion Level Difference
CE
NonCE
E
Exon Skipping: expression (Het)
p = 0.035 (*)
Log2 Fold Change
CE
NonCE
F
Exon Skipping: expression (WT)
p = 0.16 (ns)
Log2 Fold Change
CE
NonCE
G
Exon Skipping: 5'SS Strength
p = 0.048 (*)
MaxEntScan Score
Het
WT
H
Exon Skipping: 3'SS Strength
p = 0.79 (ns)
MaxEntScan Score
Het
WT
I
bits
SNRPB: SE (Het) - 5'SS
J
bits
SNRPB: SE (WT) - 5'SS
K
mRNA processing
nucleoside-triphosphatase regulator activity
chromatin binding
enzyme regulator activity
catalytic activity, acting on RNA
molecular function regulator
GTPase regulator activity
enzyme activator activity
phospholipid binding
ubiquitin-protein transferase activity
FDR
Number of Genes

Figure 4: *Snrpb*$^{ncc+/-}$ mutants show aberrant splicing that includes both increased exon skipping and intron retention. A. DEGs identified could grouped into molecular pathways belonging to the p53 signaling pathway and the spliceosome B. A much larger number of transcripts was found to be abnormally spliced in the *Snrpb*$^{ncc+/-}$ mutants. The most abundant of Differentially Spliced Exons (DSE) were skipped exons (SE) and retained introns (RI). A strong tendency towards increased exon skipping and intron inclusion in the mutant samples was observed; there were more SE (273 in Het versus 83 in WT) and RI (191 in Het versus 21 in WT). C.-F. Exon skipping was significantly higher for NonCE in the Het when constitutive (CE) vs Non-constitutive exons (Non-CE) were examined. G-J. For exon skipping, Splice site (SS) strength was significantly stronger 5'SS in mutants (P=.05). K. Pathway analysis of genes with DSEs showed that they were significantly associated with mRNA processing.

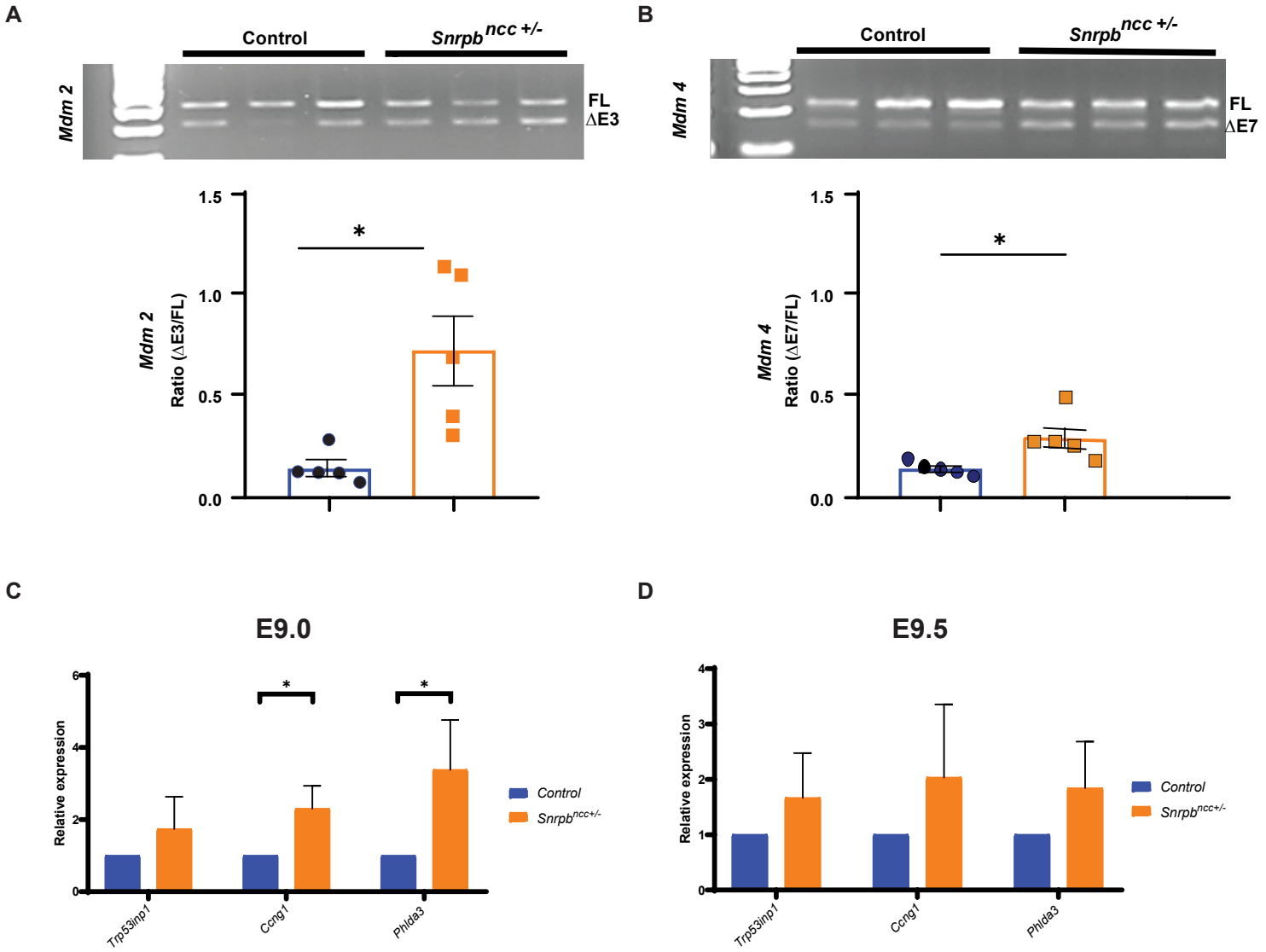
A
Control
Snrpb ncc +/-
Mdm 2
FL
ΔE3
Mdm 2
Ratio (ΔE3/FL)
1.5
1.0
0.5
0.0
*
B
Control
Snrpb ncc +/-
Mdm 4
FL
ΔE7
Mdm 4
Ratio (ΔE7/FL)
1.5
1.0
0.5
0.0
*
C
E9.0
Relative expression
6
4
2
0
*
*
Control
Snrpb ncc+/-
Trp53inp1
Ccng1
Phlda3
D
E9.5
Relative expression
4
3
2
1
0
Control
Snrpb ncc+/-
Trp53inp1
Ccng1
Phlda3

Figure 5: Increased exon skipping in two regulators of P53; *Mdm2* and *Mdm4*, and significant increases in P53-target genes in *Snrpb*$^{ncc+/-}$ mutants. A. and **B**. RT-PCR showing full length and the shorter transcripts produced in *Mdm2* and *Mdm4* as a result of increased exon-skipping, respectively, in E9.0 control and mutant embryos. When quantified, a significant increase of shorter exon was found in both *Mdm2* and *Mdm4* (t-test, $p<.05$). **C** and **D**. RT-qPCR revealed significant increases in levels of P53 target genes at E9.0 (t-test, $p<.05$) but not at E9.5. FL= full length transcript, ΔE3= transcript with exon 3 skipped, ΔE7= transcript with exon 7 skipped.

Alam Fig.6

A

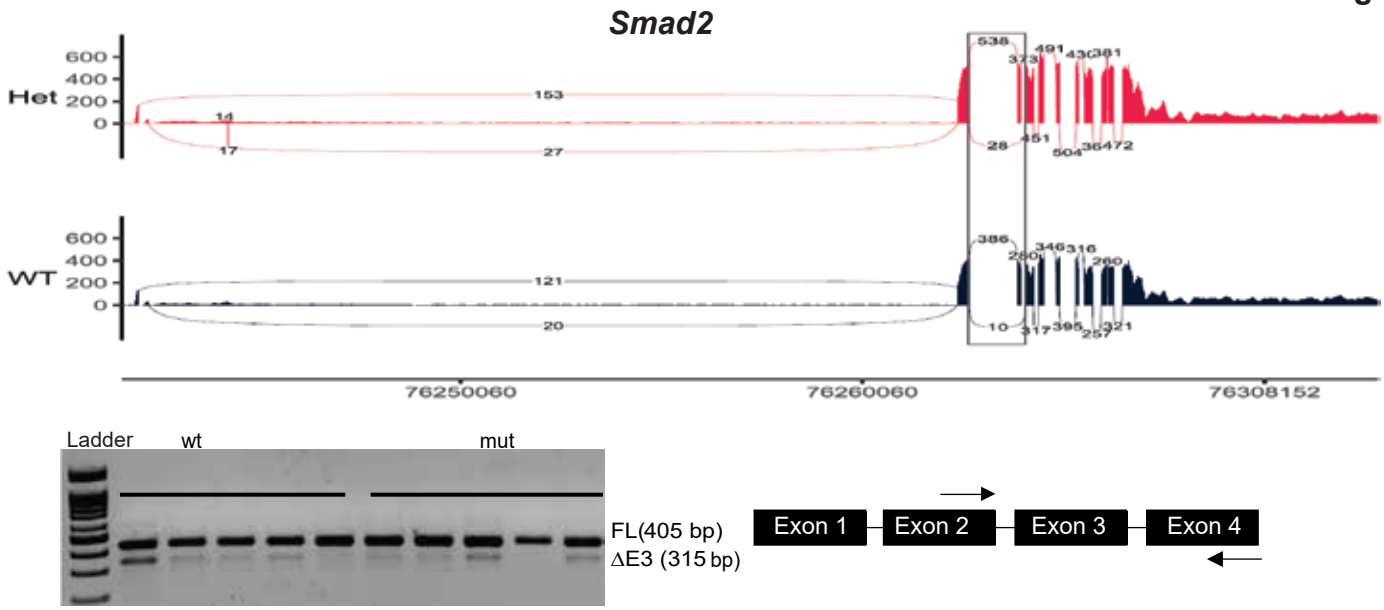

B

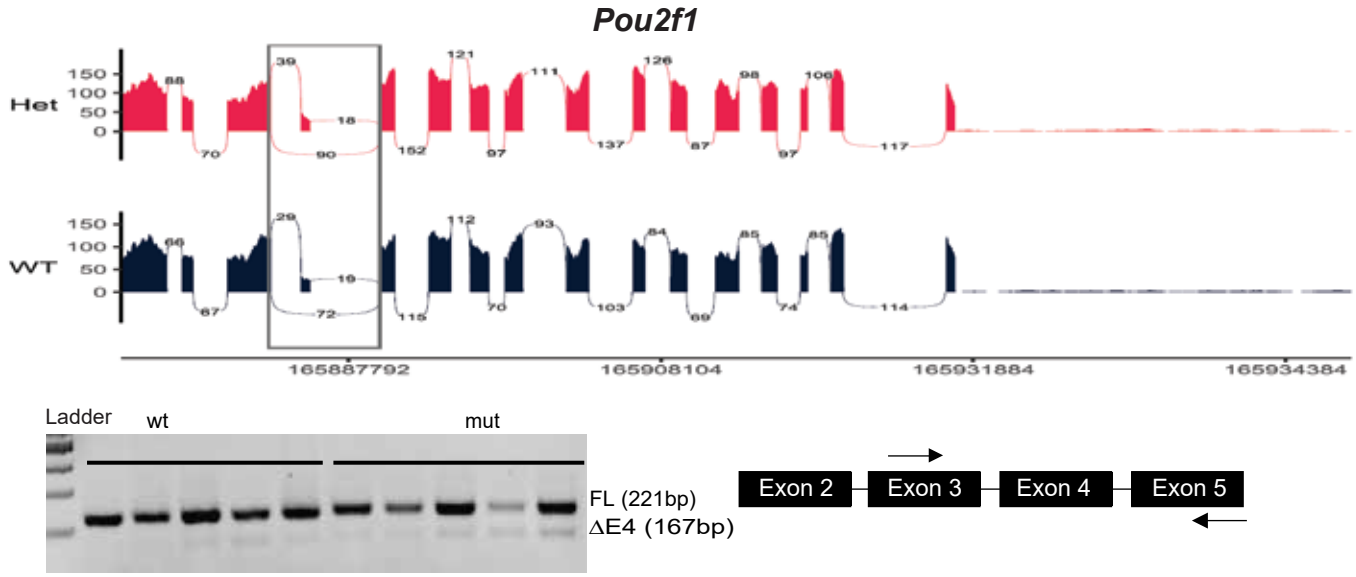

C

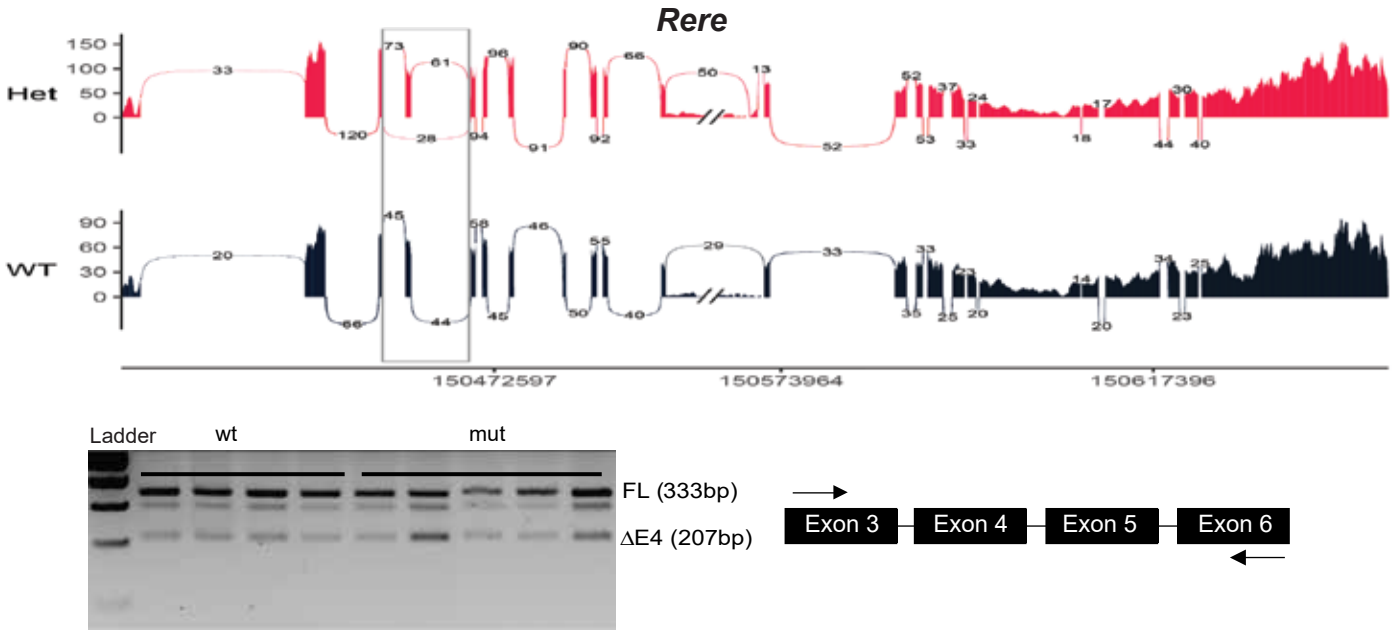

Figure 6: RT-PCR confirms exon skipping in genes important for craniofacial development in E9.0 embryos. Sashimi plot for the exon skipping events found for **A**. *Smad2,* **B**. *Pou2f1* and **C**. *Rere*. Under each sashimi plot, representative gel for RT-PCR showing the presence of transcripts with the predicted exon skipping event. Location of the primers used to amplify the transcripts is shown on the right. FL=Full length, ΔE=skipped exon.

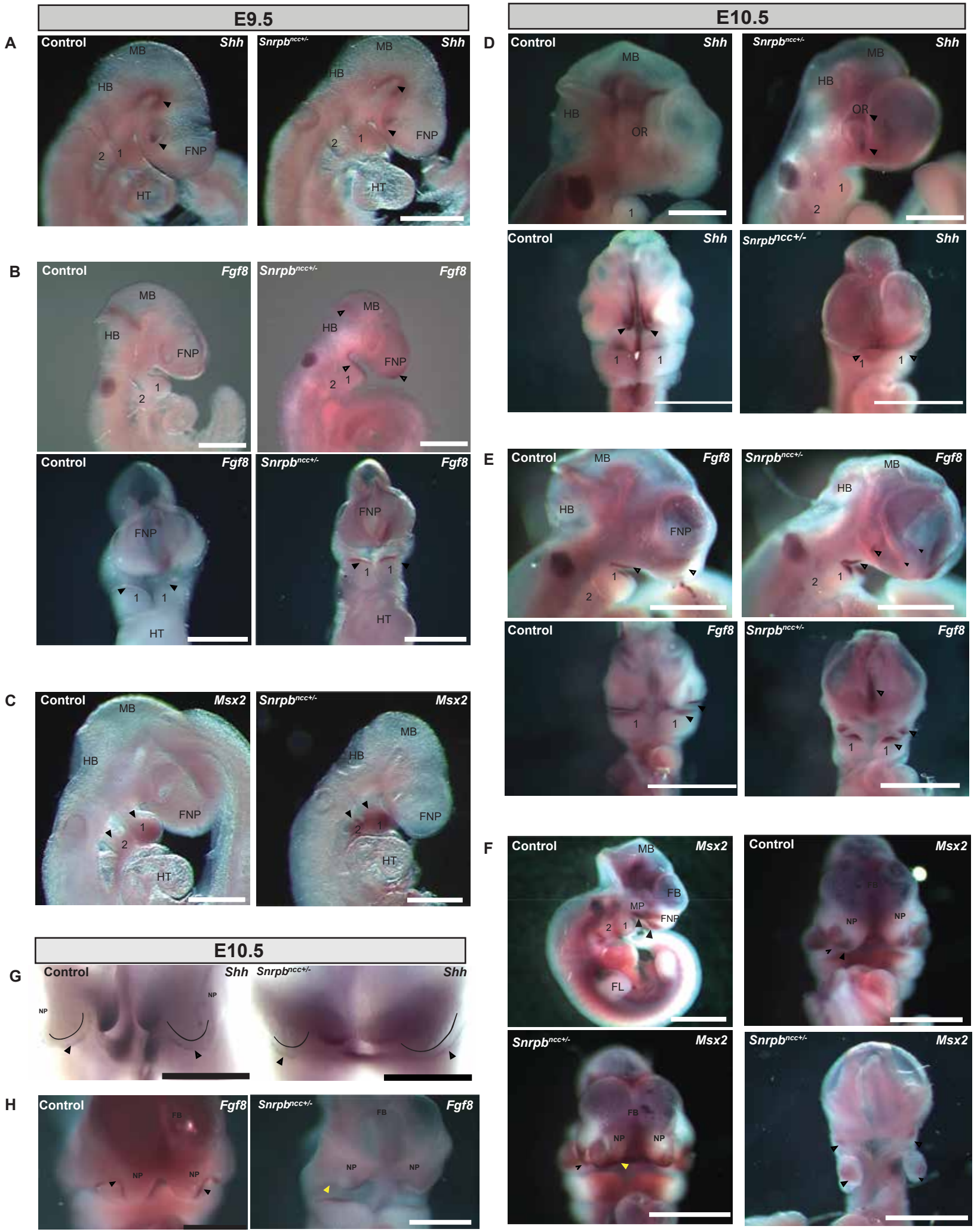
E9.5
E10.5
A
B
C
D
E
F
G
H
Control
Snrpb ncc+/-
Shh
Fgf8
Msx2
MB
HB
FNP
HT
OR
MP
FB
FL
NP
1
2

Figure 7: *Shh*, *Fgf8* and *Msx2* are mis-expressed in *Snrpb*$^{ncc+/-}$ embryos. Wholemount ISH for **A**. *Shh* at E9.5 shows expression in the ventral-most region of the neural tube, the floor plate, as well as the ventral prosencephalon of control and *Snrpb*$^{ncc+/-}$ embryos. **B**. Expression of *Fgf8* is expanded in mutant embryos at the mandibular epithelium, the frontonasal prominence, and the midbrain/hindbrain junction (arrowheads) (n=4). **C**. *Msx2* expression is extended proximally in pharyngeal arches 1 and 2 in mutants versus controls (n=2). At E10.5, wholemount ISH for **D**. *Shh* expression in the diencephalon and the ventral forebrain in control and mutant embryos. Ectopic expression is found in the dorsal and ventral optic lens (arrowheads). **E**. Top panel shows a representative lateral view of a control embryo in which *Fgf8* is detected on the surface ectoderm of the mandible, maxillary and frontonasal prominences (n=3). A representative mutant embryo with *Fgf8* expression on the mandibular ectoderm and in the region where the maxillary prominence would normally form (arrowheads, n=3). Bottom panel shows frontal view of reduced *Fgf8* expression in the lateral nasal prominence in mutants, and ectopic expression of *Fgf8* on the surface ectoderm of the medial nasal process, towards the midline (arrowhead). **F**. Top panel shows a lateral and ventral view of Msx2 expression in E10.5 control embryos. Bottom panel shows that in E10.5 Group 1 *Snrpb*$^{ncc+/-}$ mutants, *Msx2* is expressed in the lateral and medial nasal prominences, although expression appeared reduced but ventrally expanded in the medial frontal nasal region. On the right, in Group 2 *Snrpb*$^{ncc+/-}$ mutants missing the frontonasal and maxillary prominences, *Msx2* is expressed in the maxillary and in the mandibular region of the hypoplastic first arch. **G**. and **H**. Higher magnification of the FEZ region of E10.5 embryos showing **G**. *Shh* expression in the developing mandibular periderm, and bilaterally on the surface ectoderm of the medial nasal prominences (arrowheads). **H**. *Fgf8* expression in the lateral nasal prominence is reduced in mutants (yellow arrowhead), while ectopic expression of *Fgf8* is found on the surface ectoderm of the medial nasal process, towards the midline. MB=midbrain, HB=hindbrain, FNP=frontonasal process, HT=heart, 1,2=pharyngeal arches, OR=optic region, MP=mandibular process, NP=nasal process